

The Peculiar Volatile Composition of CO-Dominated Comet C/2016 R2 (PanSTARRS)

ADAM J. MCKAY,^{1,2,*} MICHAEL A. DISANTI,^{1,*} MICHAEL S. P. KELLEY,³ MATTHEW M. KNIGHT,³ MARIA WOMACK,⁴
KACPER WIERZCHOS,⁵ OLGA HARRINGTON PINTO,⁵ BONCHO BONEV,² GERONIMO L. VILLANUEVA,¹ NEIL DELLO RUSSO,^{6,*}
ANITA L. COCHRAN,⁷ NICOLAS BIVER,⁸ JAMES BAUER,³ RONALD J. VERVACK, JR.,⁶ ERIKA GIBB,⁹ NATHAN ROTH,⁹ AND
HIDEYO KAWAKITA¹⁰

¹*NASA Goddard Space Flight Center
8800 Greenbelt Rd
Greenbelt, MD, 20771 USA*

²*Department of Physics
American University
4400 Massachusetts Avenue NW
Washington, D.C., 20016 USA*

³*Department of Astronomy
University of Maryland
4296 Stadium Dr.
College Park, MD, 20742 USA*

⁴*Florida Space Institute
University of Central Florida
Partnership 1, Research Parkway
Orlando, FL, 32816 USA*

⁵*Department of Physics
University of South Florida
4202 East Fowler Ave
Tampa, FL, 33620 USA*

⁶*Johns Hopkins University Applied Physics Laboratory
11100 Johns Hopkins Rd.
Laurel, MD, 20723 USA*

⁷*University of Texas at Austin/McDonald Observatory
2512 Speedway, Stop C1402
Austin, TX, 78712 USA*

⁸*LESIA, Observatoire de Paris, Université PSL, CNRS,
Sorbonne Université, Université de Paris, Sorbonne Paris Cité
5 place Jules Janssen, F-92195 Meudon, France*

⁹*Department of Physics
1 University Blvd.
University of Missouri-St.Louis
St. Louis, MO, 63121 USA*

¹⁰*Koyama Astronomical Observatory
Kyoto Sangyo University
Motoyama, Kamigamo, Kita-ku, Kyoto, 603-8555, Japan*

(Received; Revised; Accepted July 15, 2019)

ABSTRACT

Comet C/2016 R2 (PanSTARRS) has a peculiar volatile composition, with CO being the dominant volatile as opposed to H₂O and one of the largest N₂/CO ratios ever observed in a comet. Using observations obtained with the *Spitzer Space Telescope*, NASA's Infrared Telescope Facility, the 3.5-meter

ARC telescope at Apache Point Observatory, the Discovery Channel Telescope at Lowell Observatory, and the Arizona Radio Observatory 10-m Submillimeter Telescope we quantified the abundances of 12 different species in the coma of R2 PanSTARRS: CO, CO₂, H₂O, CH₄, C₂H₆, HCN, CH₃OH, H₂CO, OCS, C₂H₂, NH₃, and N₂. We confirm the high abundances of CO and N₂ and heavy depletions of H₂O, HCN, CH₃OH, and H₂CO compared to CO reported by previous studies. We provide the first measurements (or most sensitive measurements/constraints) on H₂O, CO₂, CH₄, C₂H₆, OCS, C₂H₂, and NH₃, all of which are depleted relative to CO by at least one to two orders of magnitude compared to values commonly observed in comets. The observed species also show strong enhancements relative to H₂O, and even when compared to other species like CH₄ or CH₃OH most species show deviations from typical comets by at least a factor of two to three. The only mixing ratios found to be close to typical are CH₃OH/CO₂ and CH₃OH/CH₄. The CO₂/CO ratio is within a factor of two of those observed for C/1995 O1 (Hale-Bopp) and C/2006 W3 (Christensen) at similar heliocentric distance, though it is at least an order of magnitude lower than many other comets observed with AKARI. While R2 PanSTARRS was located at a heliocentric distance of 2.8 AU at the time of our observations in January/February 2018, we argue, using sublimation models and comparison to other comets observed at similar heliocentric distance, that this alone cannot account for the peculiar observed composition of this comet and therefore must reflect its intrinsic composition. We discuss possible implications for this clear outlier in compositional studies of comets obtained to date, and encourage future dynamical and chemical modeling in order to better understand what the composition of R2 PanSTARRS tells us about the early Solar System.

Keywords: comets — composition — planet formation —

1. INTRODUCTION

Comets are primitive, volatile-rich remnants from the formation of the Solar System, and for this reason their volatile composition is considered indicative of the physics and chemistry occurring in the protosolar disk during the planet formation stage. While there is diversity in compositions among the cometary population, comets consist primarily of H₂O, followed by CO₂ and CO at the 1-30% level, with trace species such as HCN, CH₃OH, and C₂H₆ being present at the few percent level or less (Mumma and Charnley 2011). The optical taxonomy of comets also shows diversity and evidence for modality (i.e. clumps of different compositional types), but in general optical cometary spectra are dominated by OH (and therefore H₂O), with CN, C₂, C₃, CH, NH, and NH₂ present at the percent level or less (e.g. A'Hearn et al. 1995; Cochran et al. 2012).

However, a few comets do not fit neatly into the established taxonomies. Comet 96P/Machholz shows an extremely atypical coma composition at optical wavelengths (though OH is still the dominant species), with a C₂/CN ratio an order of magnitude higher than other comets (Langland-Shula and Smith 2007; Schleicher 2008). Some comets, such as 29P/Schwassman-Wachmann 1, have observed CO/H₂O ratios $\gg 1$ (Ootsubo et al. 2012), though this is often, at least partially, explained by its heliocentric distance being beyond the water ice line where water ice does not readily sublimate, meaning the observed coma composition is not necessarily indicative of the ice composition of the nucleus (Womack et al. 2017).

Comet C/2016 R2 (PanSTARRS) was observed to have a peculiar optical spectrum when it was at a heliocentric distance of 3.1 AU, dominated by emissions from CO⁺ and N₂⁺ with a lack of emission from other species such as CN and C₂ typically observed at these wavelengths (Cochran and McKay 2018). From these observations, it was derived that N₂/CO ~ 0.06 , among the highest values observed in a comet. This result, coupled with the lack of many of the usual emissions observed in optical cometary spectra, suggested that this comet has a composition very different from any other comet observed to date. This was quickly communicated to the cometary science community for additional observations. Observations with the Arizona Radio Observatory 10-m Submillimeter Telescope (ARO SMT) confirmed a very high CO production rate and identified a low HCN abundance (Wierzechos and Womack 2017, 2018; de Val-Borro et al. 2018). Observations with the IRAM 30-meter telescope and the Nancay radio telescope provided a more complete picture of the volatile composition of R2 PanSTARRS, confirming the high CO abundance and anomalously

* Visiting Astronomer at the Infrared Telescope Facility, which is operated by the University of Hawaii under contract NNH14CK55B with the National Aeronautics and Space Administration.

low abundances of other volatiles such as HCN and H₂O compared to CO (Biver et al. 2018). Additional high spectral resolution optical observations obtained with the UVES instrument on the VLT were reported by Opitom et al. (2019), confirming the findings of Cochran and McKay (2018) as well as providing new insights such as the first detection of [N I] emission in a cometary coma.

We present analysis of IR measurements obtained with the *Spitzer Space Telescope* and iSHELL on the NASA IRTF designed to quantify a suite of species observed in comets: H₂O, CO₂, CO, C₂H₆, CH₃OH, CH₄, H₂CO, and OCS. We also present optical measurements used to study HCN (through CN emission), NH₃ (through NH₂ emission), N₂ (through N₂⁺), C₂H₂ (through C₂) and H₂O (through OH and [O I]6300 Å emission), as well as new millimeter-wavelength observations of CO that are contemporaneous with our *Spitzer* observations. Section 2 presents our observations and Section 3 presents our analysis procedures and results. Section 4 discusses this truly peculiar comet in the context of current compositional taxonomies and possible implications for the physics and chemistry of the comet-forming region during the protoplanetary disk phase. Section 5 concludes the paper and encourages future work to better understand what R2 PanSTARRS reveals about the early Solar System.

2. OBSERVATIONS

We obtained observations in late January/February 2018 with several facilities, both space-borne and ground-based. These observations are detailed in Table 1.

Table 1. Observation Log

UT Date	R _h (AU)	\dot{R}_h (km s ⁻¹)	Δ^a (AU)	$\dot{\Delta}^a$ (km s ⁻¹)	Solar Standard	Tell. Standard	Flux Standard
NASA IRTF iSHELL							
January 30, 2018	2.81	-6.8	2.27	+17.2	-	HR 1165	HR 1165
ARO SMT							
February 13, 2018	2.76	-6.0	2.41	+19.5	-	-	Chopper Wheel
<i>Spitzer</i> IRAC ^b							
February 12, 2018	2.76	-6.0	2.26	-28.4	-	-	-
February 21, 2018	2.73	-5.5	2.11	-25.9	-	-	-
DCT LMI							
February 21, 2018	2.73	-5.5	2.52	+20.3	-	-	HD 72526 HD 37112
APO ARCES							
January 30, 2018	2.81	-6.8	2.27	+17.2	Hyades 64	55 Persei	HR 1544

^aValues for Δ and $\dot{\Delta}$ are the distance to the observer and velocity relative to the observer, respectively. Therefore for *Spitzer* observations these are relative to the *Spitzer* spacecraft, while for ground-based observations these are relative to Earth.

^b*Spitzer* astronomical observation request (AOR) numbers: 65280768, 65281280, 65281024, 65281536

2.1. NASA IRTF iSHELL

We obtained Director’s Discretionary Time to observe R2 PanSTARRS with the powerful iSHELL IR spectrograph on the NASA IRTF on Maunakea, HI on UT January 29 and 30, 2018. While poor weather precluded obtaining useful data on January 29, we obtained high quality spectra on January 30. The iSHELL detector is a 2048 × 2048 pixel Hawaii H2RG array with sensitivity over a wavelength range of ~ 1-5 μm. As a cross-dispersed instrument, iSHELL measures signal in many (>10) consecutive echelle orders simultaneously with complete (for λ ≤ 4 μm) or nearly complete (for λ > 4 μm) spectral coverage, a significant improvement over the previous IRTF high-resolution facility spectrograph, CSHELL (Tokunaga et al. 1990). More details on iSHELL can be found in Rayner et al. (2012, 2016).

For our observations of R2 PanSTARRS, we used the 0.75'' wide slit, which provides a spectral resolution of $R \equiv \frac{\lambda}{\delta\lambda} \sim 38,000$ for a uniform monochromatic source. We also observed an early type IR standard star with the 4'' wide slit to serve as a flux calibrator and a telluric standard (see Section 3.1). This slit provides lower spectral resolution ($R \sim 20,000$), but minimizes slit losses and therefore systematic errors in flux calibration. Both the comet and standard star were observed using the classic ABBA nodding sequence, with a 7.5'' telescope nod (half the slit length) along the

slit between the A and B positions, located equidistant to either side of the slit midpoint. We employed two grating settings: M2 and Lp1. M2 covers a wavelength range of $\sim 4.52 - 5.25 \mu\text{m}$, encompassing spectral lines of CO, H₂O, and OCS. Lp1 covers the wavelength range $\sim 3.28-3.65 \mu\text{m}$ and targets emission from CH₄, C₂H₆, CH₃OH, H₂CO, and OH prompt emission (a well established proxy for H₂O production in comets (Bonev et al. 2006)). Our comet observations resulted in 29.2 minutes on source in M2 and 59.8 minutes on source in Lp1. We obtained flats and darks at the end of each observing sequence for each grating setting.

Guiding was achieved through filter imaging with the slit-viewer camera, performed in specific wavelength bands independent of the wavelength regime used to obtain spectra. The slitviewer allows active guiding on sufficiently bright targets while obtaining spectra. Short time-scale guiding is achieved through a boresight guiding technique, which utilizes “spillover” flux that falls outside the slit to keep the optocenter on the slit. However, while easily visible in the guider using a broadband J filter, R2 PanSTARRS was not bright enough for active guiding. We instead performed offset guiding using a reference (guide) star in the slitviewer field of view (FOV). Owing to the small non-sidereal rates of R2 PanSTARRS, this worked very well; we verified that the comet’s position with respect to the slit remained very stable over the course of our observations, with minimal adjustments needed to keep it in the slit. More details relevant to cometary observations using iSHELL are presented in DiSanti et al. (2017).

2.2. Arizona Radio Observatory Sub-millimeter Telescope (SMT)

Observations of the CO(2-1) line at 230.53799 GHz were performed with the Arizona Radio Observatory 10-m Submillimeter Telescope on 2018 February 13 at 5:16 UT using the 1.3 mm dual polarization receiver with ALMA Band 6 sideband-separating mixers. The observations began 11 hours after the first *Spitzer* epoch. Data acquisition was done in beam-switching mode with a $+2'$ throw in azimuth and standard 6 minute scans were acquired. System temperatures had peak values of 390K, but on average remained under 340K. The chopper wheel method was used to determine the temperature scale for the SMT receiver systems with a beam efficiency of $\eta = 0.74$. The backend configuration that provided the best velocity resolution (0.325 km s^{-1} per channel) consisted of a 2048 channel 250 kHz/channel filterbank in parallel mode. Accuracy of the pointing and tracking was checked against the JPL Horizons ephemeris position and was found to be better than $< 1''$ rms. Due to high winds, only 12 scans were obtained but the CO line was strong enough to be seen in single scans.

2.3. *Spitzer* IRAC

We obtained Director’s Discretionary Time to observe R2 PanSTARRS with *Spitzer* IRAC on 2018 February 12 at 18:22 UT and 2018 February 21 at 01:03 UT in order to measure the CO₂ production rate. As *Spitzer* is well into its post-cryogenic mission, IRAC presently observes in two pass bands: one centered at $3.6 \mu\text{m}$ and the other at $4.5 \mu\text{m}$. Both filters have broad wavelength coverage, with bandwidths of 0.8 and $1.0 \mu\text{m}$, respectively. The $4.5 \mu\text{m}$ band has been used extensively in the past for measuring CO₂ production rates in comets, as this bandpass includes the ν_3 band of CO₂ at $4.26 \mu\text{m}$ (e.g. Reach et al. 2013; McKay et al. 2016). It also contains the $\nu(1-0)$ band of CO at $4.7 \mu\text{m}$, but in many comets in the AKARI survey (Ootsubo et al. 2012), the CO₂ feature was at least 10 times brighter than the CO feature, and so CO₂ is typically assumed to be the dominant gas emission feature in the IRAC $4.5 \mu\text{m}$ band. This is due to the fluorescence efficiency of CO₂ being approximately an order of magnitude larger than that for CO coupled with the fact that the CO₂ abundance in comets is often equal to or greater than the CO abundance. There are examples, however, such as C/2006 W3 (Christensen) and 29P/Schwassman-Wachmann 1, where CO emission contributes significantly to the $4.5 \mu\text{m}$ band flux (Ootsubo et al. 2012; Reach et al. 2013). The high CO production rate found for R2 PanSTARRS (Wierchos and Womack 2018; de Val-Borro et al. 2018; Biver et al. 2018) means CO emission may not be negligible in the *Spitzer* imaging, and may in fact dominate signal in the $4.5 \mu\text{m}$ channel. We discuss how we account for the CO contribution in the *Spitzer* imaging in Section 3.3.

We supply details of our observations in Table 1. The IRAC array is a 256×256 pixel InSb array, covering a $5.2' \times 5.2'$ FOV with a spatial scale of $1.2''/\text{pixel}$, which for our observations corresponds to a projected FOV of $\sim 500,000 \text{ km}$ and a spatial scale of $\sim 1900 \text{ km}/\text{pixel}$. We employed a 9-position random dither pattern. Each bandpass is observed with independent arrays, such that when one array is observing the comet, the other is on an adjacent field. The sequence takes about 12 minutes to execute. For each epoch we performed observations of the comet field several days after each cometary observation in order to image the field without the comet in it. These images are termed “shadow observations” and provide a measurement of the background to be subtracted from the cometary images.

Our observations were obtained in high dynamic range (HDR) mode, which entailed obtaining exposures with both short (1.2 s) and long (30 s) exposure times in order to avoid saturation of the inner coma, while still keeping high signal-to-noise ratio (SNR) in the fainter outer coma. Observing in HDR mode also helps protect against saturation due to bright field stars. For these observations no pixels were saturated; therefore to optimize SNR we analyzed the longest exposure time images.

2.4. *Discovery Channel Telescope-Large Monolithic Imager, (LMI)*

We observed R2 PanSTARRS with the Large Monolithic Imager (LMI) on the 4.3-m Discovery Channel Telescope (DCT) at Lowell Observatory from 2:51–4:13 UT on February 21, 2018. The observations were a Target of Opportunity (ToO) request that interrupted normal observations and began within 2 hours of the *Spitzer* observations in order to provide a near-simultaneous constraint on the water production of R2 PanSTARRS. DCT ToO requests are limited to 2 hr, which allowed us sufficient time to focus the instrument, observe high and low airmass standard stars (listed in Table 1), and obtain ~ 83 minutes on R2 PanSTARRS. Conditions were photometric with seeing $\sim 1.2''$. The comet was $\sim 33^\circ$ from a 26% illuminated moon, although no stray light attributable to the moon was evident in any of our images. The comet’s airmass ranged from 1.06 to 1.23.

LMI has a $12.3' \times 12.3'$ field of view and $6.1\text{K} \times 6.1\text{K}$ e2v CCD. On-chip 3×3 binning resulted in a pixel scale of $0.36''/\text{pixel}$. We obtained images using a standard broadband SDSS- r' filter and narrowband ion (CO^+ central wavelength/bandpass width= $4266 \text{ \AA}/64 \text{ \AA}$), gas (OH 3090/62, CN 3870/62), and dust continuum (UC 3448/84, BC 4450/67) filters that are all part of the comet Hale-Bopp set (Farnham et al. 2000). Single frames were acquired at the start and end of the sequence in the two filters with the highest signal-to-noise, r' (30 s) and CO^+ (300 s). In between, sets of exposures were acquired in OH (3 exposures each of 600 s), UC (3×300 s), and BC (2×120 s), with the sets proceeding from shortest to longest wavelength in order to minimize the effects of atmospheric extinction as the airmass increased. A single CN exposure (180 s) was also acquired at the end of the sequence. The telescope followed the comet’s ephemeris rate for all comet images.

2.5. *Apache Point Observatory-ARCES*

We obtained Director’s Discretionary Time to observe R2 PanSTARRS with the ARCES instrument on the Astrophysical Research Consortium (ARC) 3.5-meter telescope at Apache Point Observatory (APO) in Sunspot, NM on UT January 30, 2018, just hours before the iSHELL observations. ARCES provides a spectral resolving power of $R = 31,500$ and a spectral range of $3500\text{--}10,000 \text{ \AA}$ with no interorder gaps. More specifics for this instrument are discussed elsewhere (Wang et al. 2003).

Observational details are described in Table 1. For all observations we centered the $1.6'' \times 3.2''$ slit on the optocenter of the comet. We obtained six spectra of 1800 s each over the course of the night. These spectra were averaged after extraction and calibration to increase SNR. We obtained an ephemeris generated from JPL Horizons for non-sidereal tracking of the optocenter. For short time-scale guiding, the guiding software employs a boresight technique to keep the optocenter centered in the slit. We observed a G2V star in order to remove the underlying solar continuum and Fraunhofer absorption lines, a fast rotating ($v \sin(i) > 150 \text{ km s}^{-1}$) B star to account for telluric features, and spectra of a flux standard to establish absolute intensities of cometary emission lines. The calibration stars used are given in Table 1. We obtained spectra of a quartz lamp for flat fielding and acquired spectra of a ThAr lamp for wavelength calibration.

3. DATA ANALYSIS AND RESULTS

3.1. *IRTF-iSHELL*

Figure 1 shows raw spectral-spatial difference frames (total A-beam minus B-beam exposures) of R2 PanSTARRS for our M2 (left) and Lp1 (upper right) observing sequences. We applied our general methodology for processing IR spectra (e.g. Dello Russo et al. 2006; Villanueva et al. 2011; DiSanti et al. 2014). New techniques specific to iSHELL are described in detail in DiSanti et al. (2017) (see also Roth et al. (2018)). We provide a brief summary of our reduction procedures below.

Processing of each iSHELL order produces a “rectified” spectral-spatial frame, meaning each column pertains to a unique wavelength and each row to a unique spatial location along the slit. An example is shown in Figure 1 for the region of Lp1 order 157 containing the cometary R0 and R1 lines of CH_4 (panel (e), bottom-right). Such

rectified orders consist of three parts: the bottom and top thirds show comet signal obtained from A-beam and B-beam observations, respectively (in black), and the middle third shows the combined signal $[(A+B)/2]$ (in white). Spectral extracts for the standard star and comet are obtained by summing signal over a range of rows in the central (combined-beam) portion of their rectified frames.

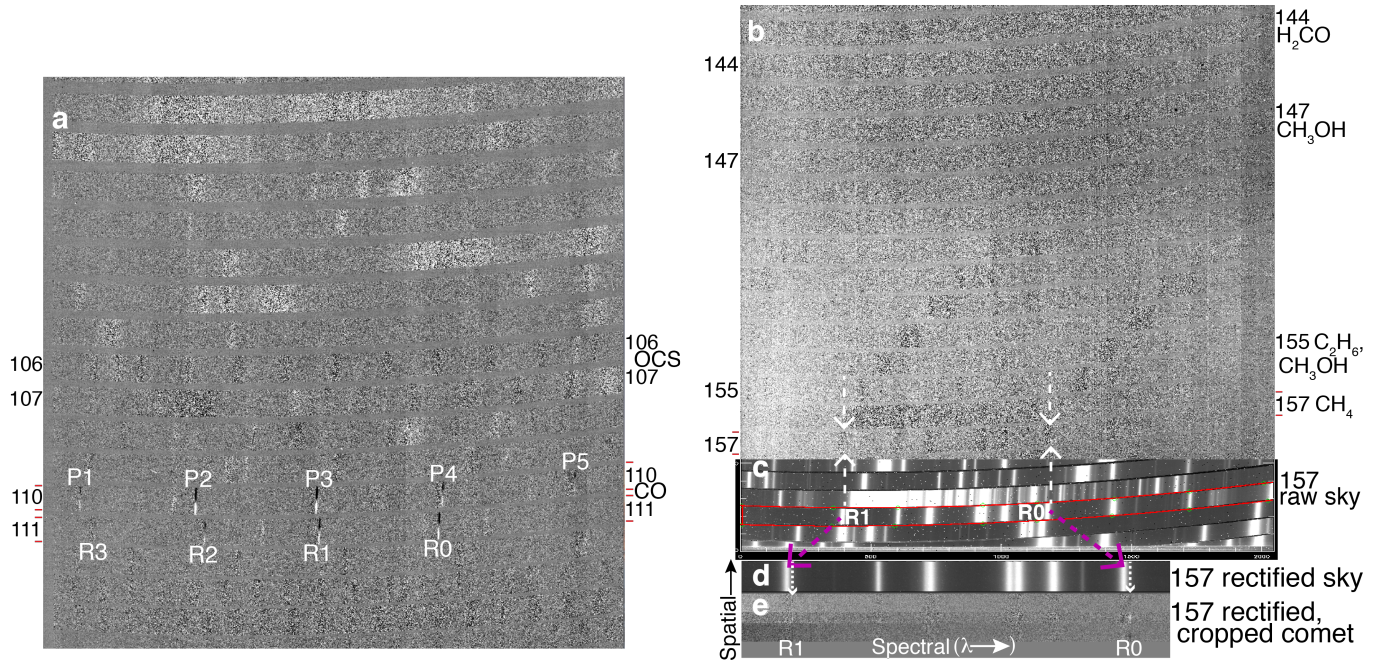


Figure 1. Raw spectral-spatial stacks (A-B difference frames) of R2 PanSTARRS obtained with iSHELL in the (a) M2 and (b) Lp1 settings on UT 30 January 2018, with echelle orders relevant to our study indicated (106, 107, 110 and 111 for M2; 144, 147, 155, and 157 for Lp1), and with molecules targeted in each order listed at right. CO emission lines (labeled with their rotational designations) are clearly seen in M2 orders 110 and 111, with the A-beam signal in white and the B-beam signal in black. Conversely, no emission lines are readily apparent in the Lp1 stack. (c) Portion of the corresponding Lp1 raw sky frame that includes order 157, outlined in red and spectrally aligned with the raw comet stack. Expected positions of the cometary CH_4 lines are depicted by vertical white dashed arrows immediately to the right/red of the corresponding sky emission lines, in accordance with the geocentric velocity of R2 PanSTARRS ($\dot{\Delta} = +17.2 \text{ km s}^{-1}$; Table 1). (d) Sky emission centered around the CH_4 lines in order 157, after being rectified as explained in the text. (e) Corresponding rectified order for R2 PanSTARRS, again with the cometary CH_4 lines Doppler-shifted from their telluric counterparts. The combined comet signal (in white) is shown as the middle portion and, above and below this (in black) individual B- and A-beams, respectively. For spectral extracts from the CO and CH_4 orders, see Fig. 2.

To achieve absolute flux calibration, and to determine the column burdens of absorbing species in the terrestrial atmosphere, we fit a synthetic atmospheric transmittance model to the standard star spectrum for each processed order. We applied this optimized atmospheric transmittance model (calculated at the airmass of R2 PanSTARRS), convolved it to the spectral resolution of the cometary observations and scaled it to the cometary continuum level (the continuum is virtually absent for our observations of R2 PanSTARRS). Subtracting the scaled model yields the net observed cometary emission spectrum, still multiplied by monochromatic atmospheric transmittance at the Doppler-shifted frequency of each cometary line. Correcting for transmittance and incorporating flux calibration factors from our standard star spectra allows establishing line fluxes incident at the top of the terrestrial atmosphere. Fully calibrated spectral extracts for R2 PanSTARRS showing emission lines of CO and CH_4 are shown in Figure 2. All other species searched for were not detected.

We establish molecular column densities (or upper limits) by dividing these transmittance-corrected line fluxes by appropriate line-specific fluorescence g-factors, the values of which depend on rotational temperature (T_{rot}). For our study of R2 PanSTARRS with iSHELL, only CO presented enough lines with high signal-to-noise that spanned a sufficient range of rotational energy to obtain a measure of T_{rot} . Because the solar spectrum contains CO absorption lines,

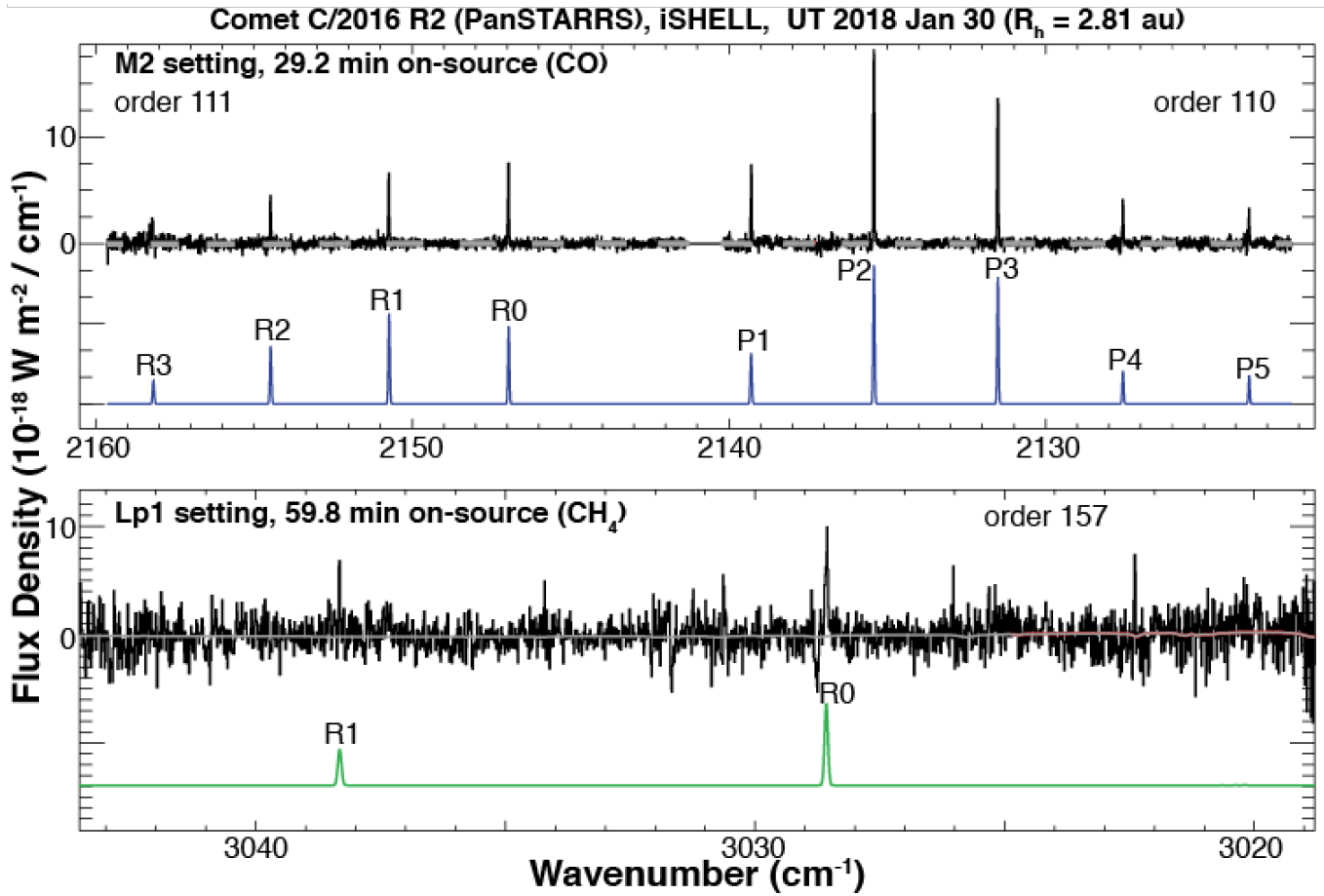


Figure 2. Spectra and corresponding fluorescence model fits to observed CO (top) and CH_4 (bottom) emission in R2 PanSTARRS obtained with iSHELL. Each spectrum represents the signal summed over 15 rows ($2.25''$) centered on the peak emission, and each line is labeled with its rotational identification. We detected nine CO lines spanning two echelle orders, and two CH_4 lines within a single order.

an accurate treatment required using “reduced” CO g-factors that incorporate the Swings effect for the heliocentric velocity of the comet at the time of our observations (-6.8 km s^{-1} ; see Table 1). Our analysis of CO provided a best-fit value $T_{rot} = 13 \pm 2 \text{ K}$. We assume this temperature also applies to other species, as observations of brighter comets in which T_{rot} was measured for multiple species demonstrate that this is generally a valid assumption (e.g. Dello Russo et al. 2011; Mumma et al. 2011; Gibb et al. 2012; DiSanti et al. 2014).

We obtained molecular production rates as follows. We extracted a “nucleus-centered” spectrum by summing signal over 15 rows ($\sim 2.5''$) centered on the row containing the peak emission line intensity. Application of Swings-corrected g-factors and geometric parameters (R_h , Δ , beam size at the comet) to transmittance-corrected line fluxes provides the nucleus-centered production rate, Q_{nc} . However, owing primarily to seeing, Q_{nc} invariably underestimates the actual “total” (or “global”) production rate, Q_{tot} . To obtain Q_{tot} we multiplied each Q_{nc} by an appropriate growth factor (GF), determined through the well-documented “Q-curve” method for analyzing spatial profiles of emissions (Dello Russo et al. 1998). For each spatial step, a “symmetrized” Q-curve was produced by averaging signal at equal but diametrically opposed distances from the nucleus. For our observations, only CO and CH_4 were detected. Each showed bright enough emissions to allow a reliable Q-curve analysis to be performed.

We present spatial profiles and symmetrized Q-curves for CO and CH_4 in Fig. 3. For each Q-curve, GF is depicted graphically as the level of the upper horizontal line (representing Q_{tot}) divided by that of the corresponding lower horizontal line (representing Q_{nc}). We refer to the region of the coma over which Q_{tot} is measured as the “terminal region.”

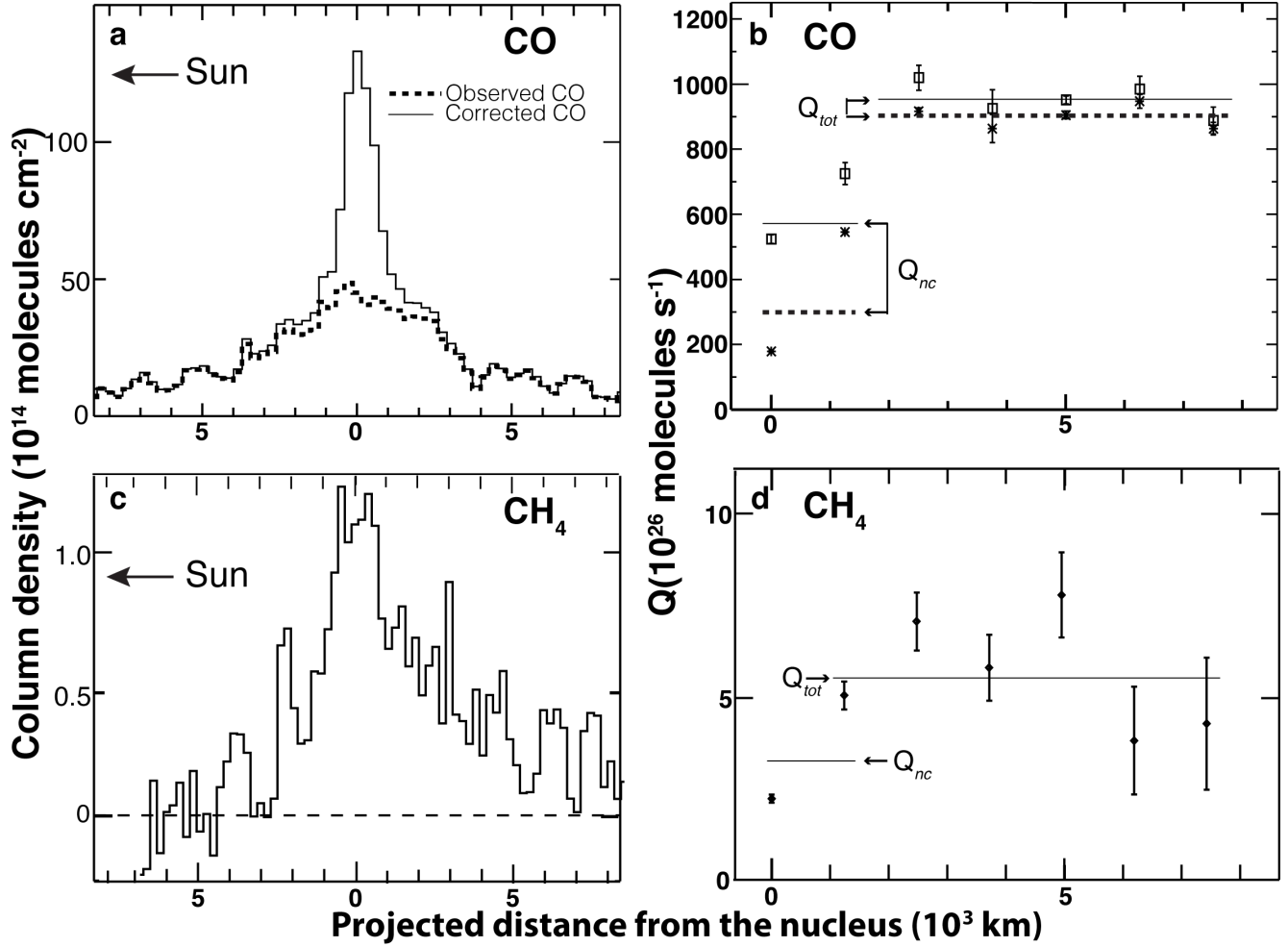


Figure 3. Spatial profiles (left) and symmetrized Q-curves (right) from our iSHELL observations of R2 PanSTARRS, representing the sum of 9 CO lines (top) and the sum of 2 CH₄ lines (bottom). For the spatial profiles, the sunward-facing hemisphere is to the left as indicated. For CO (panels a and b), dashed traces/lines represent observed emission while solid traces/lines represent emission after correcting line-by-line for optical depth in the solar pump, following the methodology of DiSanti et al. (2001). In all cases, GF is given by the ratio of total Q (Q_{tot} , upper horizontal line) to nucleus-centered Q (Q_{nc} , corresponding lower horizontal line). The GF for CO prior to correcting for optical depth (2.93 ± 0.04) is much larger than that measured for (optically thin) CH₄ (1.70 ± 0.19). However, the opacity-corrected CO Q-curve has a much lower GF = 1.67 ± 0.04 , consistent with that for CH₄. We note that for CO our formalism for correcting optical depth increases Q_{nc} by 91%, but increases Q_{tot} by only 5.6% (well within $1-\sigma$ uncertainty; see Table 3). This suggests that our approach for modeling optical depth, coupled with the Q-curve formalism, provides robust production rates for these two species in R2 PanSTARRS.

Comparison of the profiles in Fig. 3 reveals a relatively broad (and in particular a “flat-topped”) spatial distribution for the observed CO emission. This is demonstrated by its much larger GF compared to CH₄, and also that leveling its Q-curve required beginning two steps from the nucleus instead of one step, as was used for CH₄. This could indicate extended release of CO (e.g., from grains) in the inner coma, and/or optical depth in the CO lines (particularly along lines-of-sight passing close to the nucleus). The high CO production rates reported from millimeter observations of R2 PanSTARRS with IRAM (Biver et al. 2018) and SMT (Wierzos and Womack 2018), as well as from our iSHELL observations (see Table 3) suggest the IR lines of CO are affected by optical depth.

Several previous CO-rich comets revealed optically thick emissions that in all cases were most pronounced for lines-of-sight passing through the innermost coma. For observations of C/1995 O1 (Hale-Bopp) and C/1996 B2 (Hyakutake) with CSHELL at the IRTF, observed column densities and Q-curves were corrected for opacity in the solar pump assuming uniform gas outflow at constant speed (DiSanti et al. 2001, 2003). Observations of C/2006 W3

(Christensen) with CRIRES at the ESO/VLT (Bonev et al. 2017) at a similar observing geometry to our observations of R2 PanSTARRS also revealed optically thick CO for a production rate only slightly lower than has been reported for R2 PanSTARRS. Bonev et al. (2017) developed a formalism for addressing optical depth effects in CO emission based on a curve-of-growth analysis, demonstrating through their Q-curve analysis that the effects of optical depth on retrieved production rates can be quantified (and thus corrected for).

Provided that signal in the terminal region (i.e., the ends of the slit farthest from the comet optocenter) approximates optically thin conditions, the Q-curve will level out, as was observed for these three previously observed CO-rich comets, and as we also observed for R2 PanSTARRS (Fig. 3). Although in this case for CO the central region is optically thick, the GF still allows establishing a reliable approximation of the actual Q_{tot} , but with the GF for CO being significantly larger than the corresponding value for the optically thin CH_4 emission in R2 PanSTARRS (see Fig. 3). For all these comets (including R2 PanSTARRS), $Q_{tot}(\text{CO})$ as retrieved from optically thin and optically thick treatments are in formal agreement (i.e., they agree to within their respective $1-\sigma$ uncertainties); see Fig. A4 of DiSanti et al. (2001), Fig. 4 of DiSanti et al. (2003), and Fig. 4 of Bonev et al. (2017). We demonstrate this by applying the methodology detailed in the Appendix of DiSanti et al. (2001) to the observed CO emission in R2 PanSTARRS. The presence of optically thick CO emission in R2 PanSTARRS is supported by the much larger GF for the observed CO profile (2.93 ± 0.04) versus that for (optically thin) CH_4 (1.70 ± 0.19), a discrepancy that is resolved by correcting for optical depth in the CO lines (resulting in 1.67 ± 0.04 , see Fig. 3b). Therefore we conclude that our Q-curve analysis for CO mitigates the effects of optical depth on our measured CO production rate. It also reinforces our decision to apply its “corrected” GF (1.7) to obtain a realistic upper limit for co-measured OCS, and similarly to constrain Q_{tot} using the (identical within $1-\sigma$ uncertainty) GF from CH_4 for co-measured, undetected species included in the Lp1 setting (C_2H_6 , CH_3OH , and H_2CO). Derived production rates and mixing ratios are shown in Table 3.

Our spatial profiles also permit testing for asymmetric gas outflow in the coma. This is very pronounced for CH_4 (Fig. 3c), indicating a large enhancement in the anti-sunward facing hemisphere, particularly considering the relatively small solar phase angle of R2 PanSTARRS at the time of our observations ($\sim 19^\circ$) and thus the potential high degree of projection onto the sky plane. The column density of CH_4 averaged between $\sim 2,000$ and $8,000$ km from the nucleus (projected on the sky) is a factor of 2.65 ± 0.55 larger in the anti-sunward direction compared to the solar direction, while the CO profile is much more symmetric, its corresponding ratio being only 1.03 ± 0.02 .

It is possible that the asymmetry observed for CH_4 is associated with rotation of the nucleus. However, for the measured gas speed v_{exp} of 0.52 km s^{-1} (from our SMT observations, see Section 3.2) the time required to exit the iSHELL terminal region (extending to $4.9''$ from the nucleus) is approximately 4.3 hours, longer than the clock times encompassed by our M2 and Lp1 sequences (obtained consecutively and together spanning 2.65 hours of elapsed clock time). This suggests that gas in the iSHELL slit was not replenished (at least significantly) between M2 and Lp1 observations, and thus the large differences in the degrees of asymmetry observed for CO and CH_4 cannot be explained by temporally variable outgassing. Nonetheless, these results indicate that the abundance ratio CH_4/CO was higher in the anti-sunward-facing hemisphere than in the sunward-facing hemisphere by a factor of ~ 2.5 and therefore, assuming little to no replenishment of coma gas between M2 and Lp1 sequences, this implies a significantly higher CH_4/CO abundance ratio in the anti-sunward direction at the time of our iSHELL observations.

3.2. ARO-SMT

Figure 4 shows the spectrum resulting from coadding all 12 scans on UT February 13. We calculated the column density assuming optically thin gas (appropriate for the relatively large beam diameter of $32''$) with $T_{rot}=23\text{K}$ (Biver et al. 2018, see Section 4 for discussion of difference with iSHELL), and we calculated the production rate assuming a simple symmetric outflow expansion model with $V_{exp}=0.52 \text{ km s}^{-1}$ consistent with our spectra and other detailed modeling of the spectral line profiles (Wierzos and Womack 2018; Biver et al. 2018). We adopt this expansion velocity for all analysis in this work. The CO production rate is $(5.5 \pm 0.89) \times 10^{28} \text{ mol/s}$ (see Table 3).

3.3. Spitzer IRAC

We combined all images of the same exposure time using the MOPEX software (Makovoz and Khan 2005). This process creates a mosaic in the rest frame of the comet from the individual images, averaging overlapping data together, but ignoring cosmic rays and bad pixels. Two mosaics are created: one for the comet data, the other for the shadow (background) data. We subtracted the shadow mosaic from the comet mosaic to remove the background. This includes zodiacal light and celestial sources. While this removes background stars and most of the sky background, it may not

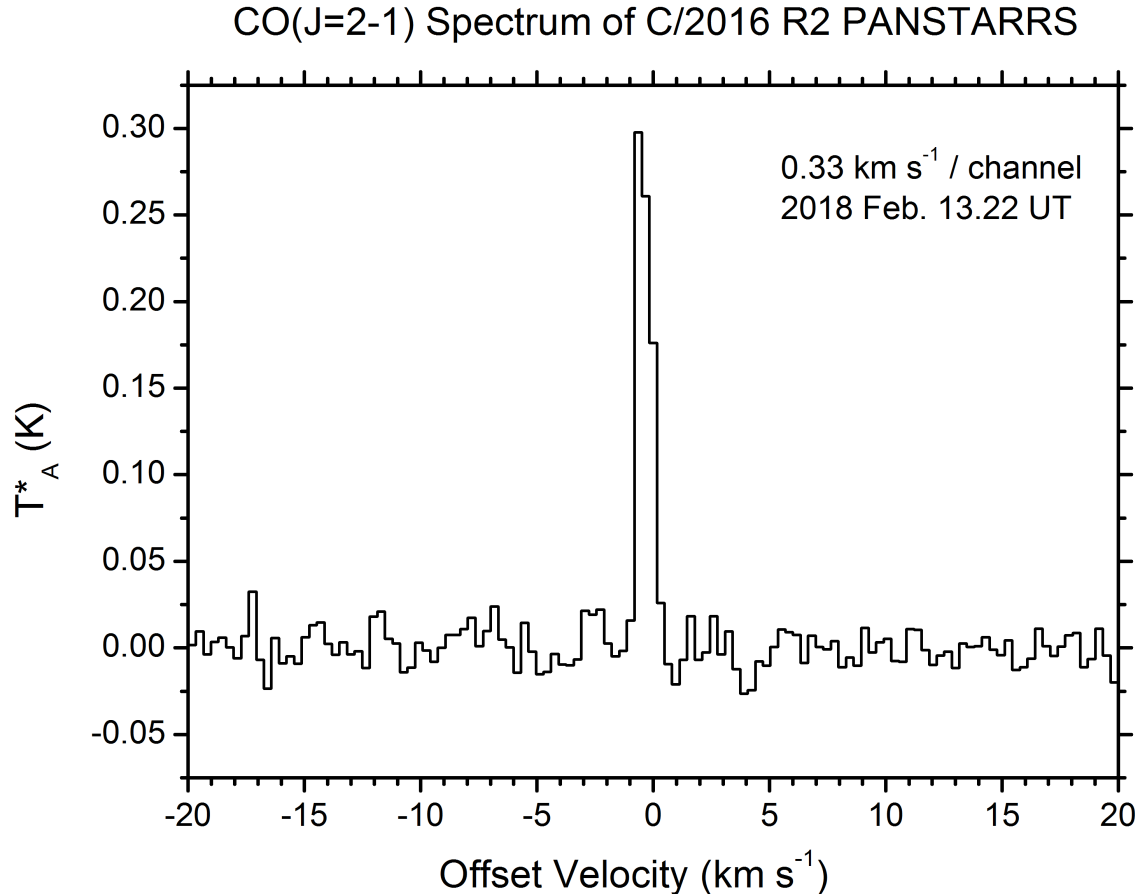


Figure 4. Spectrum of CO J=2-1 emission from comet C/2016 R2 obtained with the ARO SMT 10-m telescope on Feb. 13.22 2018 UT.

completely remove the sky background (for instance, zodiacal light for a given RA and Declination varies with time). We used the sky value from the adjacent image of blank sky to remove any residual background that remained after shadow subtraction. The resulting images are shown in the first two columns of Fig. 5.

After the mosaic images were created and the sky background was subtracted, we removed the dust contribution from the $4.5 \mu\text{m}$ band flux, isolating the gas emission. As the level of dust contamination is minimal as inferred from the $3.6 \mu\text{m}$ image being much fainter than the $4.5 \mu\text{m}$ image (see Fig. 5), we simply applied a scaling factor of 0.9 to the $3.6 \mu\text{m}$ image and subtracted it from the $4.5 \mu\text{m}$ image to remove the dust contribution from the $4.5 \mu\text{m}$ image. The scale factor of 0.9 was derived from a model for cometary dust accounting for the expected contributions of reflected light and thermal emission at the heliocentric distance of R2 PanSTARRS, based on the empirical coma dust model of Kelley et al. (2016) and the dust color of comet 67P/Churyumov-Gerasimenko at 2.8 au (Snodgrass et al. 2017). The resulting dust-subtracted images are shown in the right center column of Fig. 5. The right-most column of Fig. 5 shows the dust-subtracted images normalized by a ρ^{-1} surface brightness distribution, where ρ is the projected distance to the peak brightness, which enhances coma asymmetries. The enhanced images show strong spiral structures as well as an ion tail that we attribute to CO^+ (see Section 4). A more detailed analysis of the coma morphology is beyond the scope of this paper.

As mentioned in Section 2.3, CO likely contributes significant flux to the *Spitzer* $4.5 \mu\text{m}$ channel, especially considering the large CO production rates measured for R2 PanSTARRS at millimeter-wavelengths (Wierzbos and Womack 2018; Biver et al. 2018) and in the IR with iSHELL (Fig. 3b). CO_2 is also observed with strong emission at this wavelength in many comets (Ootsubo et al. 2012), with few other likely contributors (see Section 4 for a discussion of other possible contaminating species). Therefore, we assume that the gas emission at $4.5 \mu\text{m}$ predominantly arises

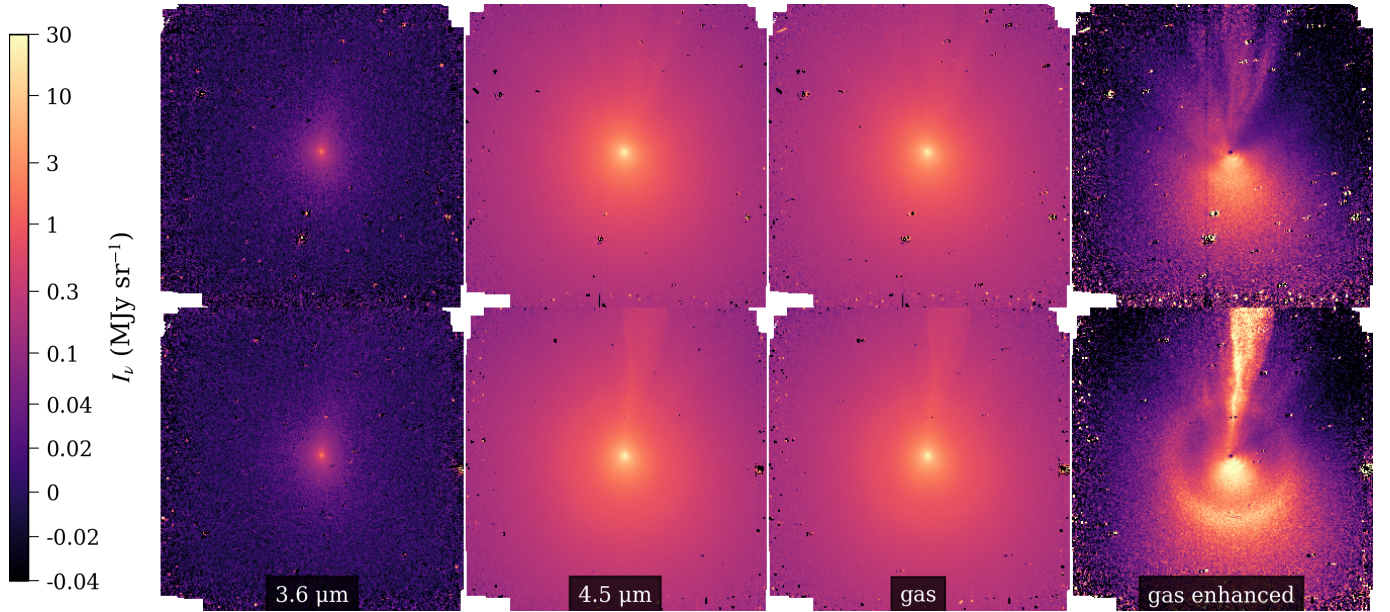


Figure 5. Shadow-subtracted images of C/2016 R2 (PanSTARRS) obtained with Spitzer IRAC at $3.6 \mu\text{m}$ (leftmost column) and $4.5 \mu\text{m}$ (left middle column), as well as the dust-subtracted images (right middle column) on UT February 12, 2018 (top row) and UT February 21, 2018 (bottom row). These images are for the longer exposure time (30 s) in our HDR mode observations. The solar direction is downward in all images. The spherical coma geometry observed in the $4.5 \mu\text{m}$ channel, as well as the large flux ratio between the two filters, is indicative of a large gas contribution to the observed flux, due to CO_2 and CO . The last column shows the dust-subtracted images normalized by a ρ^{-1} surface brightness distribution, where ρ is the projected distance to the peak brightness, which enhances coma asymmetries. There is clear evidence for a strong ion tail, which we attribute to CO^+ (see Discussion). There is also a clear spiral structure in the inner-most coma indicative of a rotating jet and a large circular arc that is present on February 21 but not February 12, possibly indicative of an impulsive outgassing event in between the two observation epochs. On both dates there is broad sunward enhancement indicative of preferential outgassing from the sunward hemisphere, which is consistent with results from CO spectral line profiles and spatial mapping measured at millimeter wavelengths (Wierzechos and Womack 2018; Biver et al. 2018). A more detailed analysis of the coma morphology is beyond the scope of this paper and will be deferred to a future publication.

from CO and CO_2 , and separate their contributions with a three-step process: 1) we initially assume that 100% of the gas emission flux comes from CO molecules and derive a CO production rate, 2) subtract the contemporaneous ground-based measured CO production rate taking care to match the projected photometric aperture used for the Spitzer observations, which leaves a residual amount, and 3) then re-characterize this residual as a CO_2 production rate.

From the dust-subtracted image of gas emission, we measured the flux for apertures ranging from 10-100 pixels ($12\text{-}120''$) in radius. We converted the broadband photometry to CO line fluxes in photons following the IRAC data handbook (Laine 2015). The line fluxes were then used to calculate the total number of CO molecules inside the photometric aperture ($N_{\text{CO},100\%}$) using

$$N_{\text{CO},100\%} = 4\pi\Delta^2 F \frac{R_h^2}{g_{\text{CO}}} \quad (1)$$

where Δ is the *Spitzer*-comet distance, F is the observed photon flux, R_h is the heliocentric distance of the comet, and g_{CO} is the g-factor for excitation of the CO $1\rightarrow 0$ fundamental vibrational band, which is 2.5×10^{-4} photons s^{-1} (Debout et al. 2016). Then the production rate $Q_{\text{CO},100\%}$, is given by

$$Q_{\text{CO},100\%} = \frac{2v}{\pi\rho} N_{\text{CO},100\%} \quad (2)$$

where $N_{\text{CO},100\%}$ is the total number of CO molecules in the photometric aperture, v is the expansion velocity, and ρ is the projected radius of the photometric aperture. We assume an expansion velocity of the coma of 0.52 km/s consistent with CO line widths from our SMT observations (see Section 3.2) and with expansion velocities reported for

R2 PanSTARRS by Wierchos and Womack (2018) and Biver et al. (2018). This approach assumes a negligible effect of photodissociation on the spatial profile in the photometric aperture, which is justified as our photometric apertures are $< 10\%$ of both the CO_2 and CO photodissociation scale lengths. We calculated production rates for a variety of aperture sizes to quantify any trends in derived production rates with aperture size. Since we found the deviations between derived production rates for different aperture sizes to be minimal ($< 5\%$), for the rest of this paper we quote production rates derived using a photometric aperture that matches the projected distance at the comet of the ARO SMT observation beam (see Section 2.2). This is a 14-pixel radius on UT February 12 and a 15-pixel radius on UT February 21. This choice minimizes systematic errors when subtracting the expected CO flux from the *Spitzer* images (see below).

If we assume that all the gas flux in the *Spitzer* 4.5 μm image is due to CO and calculate its corresponding production rate using equations (1) and (2), we find $Q_{\text{CO},100\%} \sim 1.6 \times 10^{29}$ mol/s, higher than values derived from ground-based CO observations (Wierchos and Womack 2018; Biver et al. 2018; de Val-Borro et al. 2018, and this work). Therefore we conclude that CO is probably not the sole contributor to the observed flux. However, it is a major contributor and accounting for it does have a strong influence on the derived CO_2 production rate. While CO contributes significantly to the observed *Spitzer* fluxes, the excess we attribute to CO_2 is still $> 50\%$ of the observed flux, so the detection of CO_2 is robust.

To calculate Q_{CO_2} and account for the CO contribution to the *Spitzer* 4.5 μm images, we employ our contemporaneous observations of CO at mm-wavelengths obtained with the ARO SMT (section 2.2). We favor using the contemporaneous SMT results over the IRTF CO measurements from several weeks earlier for subtraction of the CO contribution from the *Spitzer* imaging in order to minimize effects due to possible comet variability. Moreover, the production rates from SMT and *Spitzer* data were obtained using the same sized photometric aperture, whereas the iSHELL observations cover a much smaller projected region of the coma, making it more sensitive to short-time scale changes in gas production such as rotational variation. This approach minimizes systematic uncertainties introduced by possible variability in the comet's activity.

We subtracted the mm-wavelength derived CO production rate, $Q_{\text{CO},mm}$ (see Section 3.2), from the derived $Q_{\text{CO},100\%}$ value, which leaves a residual production rate: $Q_{\text{residual}} = Q_{\text{CO},100\%} - Q_{\text{CO},mm}$. We attribute the residual gas production to CO_2 (see Section 4 for a discussion of other possible contaminating species). This residual production rate is then converted to Q_{CO_2} by taking advantage of the scaling relationship between production rates and fluorescence efficiencies:

$$Q_{\text{CO}_2} = Q_{\text{residual}} \frac{g_{\text{CO}}}{g_{\text{CO}_2}} \quad (3)$$

where $g_{\text{CO}_2} = 2.69 \times 10^{-3}$ photons s^{-1} (Debout et al. 2016). Using the SMT CO production rate, we derive $Q_{\text{CO}_2} = (1.0 \pm 0.1) \times 10^{28}$ mol/s (Table 3). As a demonstration of the sensitivity of our derived CO_2 production rate to the assumed value for CO , if $Q_{\text{CO}}=0$ then $Q_{\text{CO}_2} \sim 1.5 \times 10^{28}$ mol/s, while $Q_{\text{CO}}=1.0 \times 10^{29}$ mol/s (closer to the iSHELL value) results in $Q_{\text{CO}_2} \sim 6.0 \times 10^{27}$ mol/s.

Lastly, we derived the $Af\rho$ value as a proxy for the dust production based on the 3.6 μm flux levels using the same photometric aperture as for the gas photometry and assuming all the flux is solar continuum reflected off of dust particles in the coma (i.e., negligible emissions from gaseous species and no thermal emission). We follow the methodology of A'Hearn et al. (1984) to calculate $Af\rho$. We derive $Af\rho$ values of 896 ± 27 cm on February 12 and 884 ± 27 cm on February 21, very low for a comet of this activity level and heliocentric distance. We derive $\log[Af\rho/Q(\text{H}_2\text{O})] = -23.54 \pm 0.03$, $\log[Af\rho/Q(\text{CO})] = -25.79 \pm 0.04$, and $\log[Af\rho/Q(\text{CO}_2)] = -25.05 \pm 0.04$. For similar reasons discussed above, we compare $Af\rho$ to the CO production rate measured by SMT rather than IRTF.

Due to the high quality of our *Spitzer* data, uncertainties in the photometry are dominated by the absolute calibration uncertainty of *Spitzer* IRAC, which is approximately 3% (Reach et al. 2005).

3.4. DCT-LMI

The images were bias subtracted and flat-field corrected following standard practices, and all images for a given set (OH, UC, or BC) were median combined to improve signal-to-noise and mitigate background (stellar) contamination. Absolute calibrations and gas/dust decontamination for the narrowband filters were performed using extinction coefficients determined from the two standard stars and following the procedures outlined in Farnham et al. (2000), with sky values determined from regions near the corners of the CCD that appeared to be visually free of gas/dust/ions. The CN and UC images exhibited extended, filamentary structures similar to those seen with the CO^+ filter. Although

the filters were designed to isolate gas (CN) or to be a nearly emission-free continuum area (UC), the CN bandpass includes N_2^+ emission (Cochran and McKay 2018; Opitom et al. 2019) and both bandpasses contain emissions from CO^+ ions (Pearse and Gaydon 1976, and references therein). For most comets, these ions are much fainter than the intended gas and/or continuum and can be safely ignored but this is not the case for R2 PanSTARRS. We thus conclude that the features we observed are ions and that UC and CN cannot be interpreted in their normal fashion. As a result, absolute calibrations of the OH images were performed using only the BC filter to define continuum, with solar color assumed. Flux calibrated and decontaminated images are shown in Figure 6.

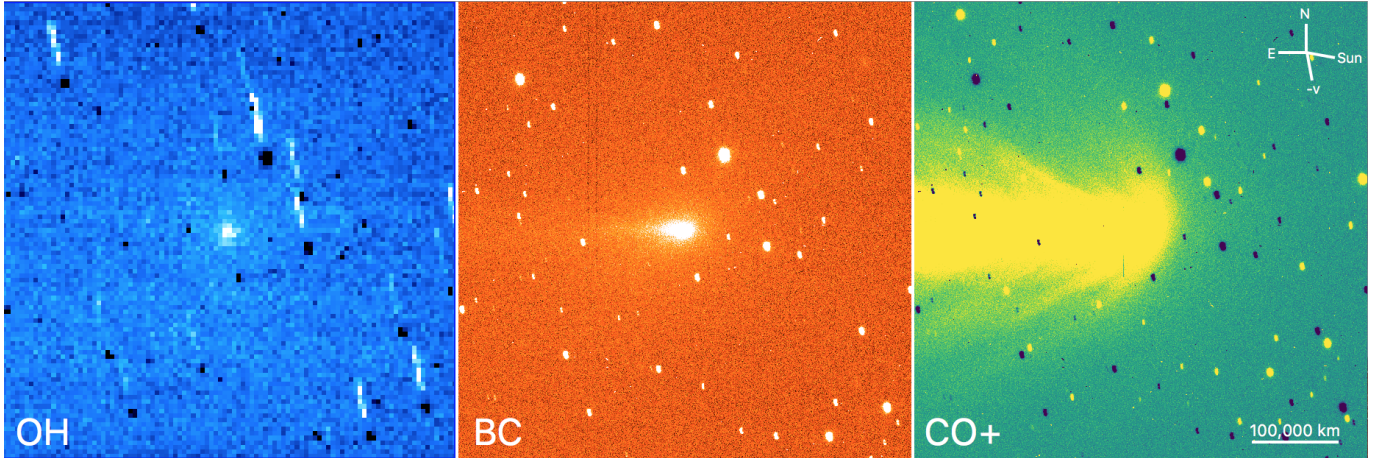


Figure 6. DCT images of OH (left, after dust and ion removal), BC (middle), and CO^+ (right, after dust removal). The OH image has been rebinned 8×8 to improve signal to noise. Background stars are visible as trailed streaks in all images, while the negative of background stars (from the continuum image) are also visible in the OH and CO^+ images as black trailed streaks. Artifacts from a bad column on the CCD are faintly seen as vertical lines on the BC and CO^+ panels. A scale bar and arrows indicating north, east, and the directions to the Sun and the heliocentric velocity vector are given on the CO^+ panel.

Our normal procedure for determining gas production rates from fully calibrated images (e.g., Knight and Schleicher 2015) is to measure the flux in a circular aperture centered on the central condensation and convert to a production rate using a Haser model and standard assumptions about the appropriate lifetimes and scale lengths (A’Hearn et al. 1995). However, we elected to perform a more complex analysis, detailed below, due to several factors. First, the low signal-to-noise of our “pure” OH image meant that trailed stars or their negative residuals from the continuum image which was removed could significantly impact our inferred OH signal. Second, the aforementioned difficulties in decontaminating the image may have potentially led to over- or under-removal of sky background and/or underlying dust continuum. Finally, we identified four lines of CO^+ from the $A^2\Pi - X^2\Sigma$ “comet-tail system” (Pearse and Gaydon 1976, and references therein) that fall in the OH filter bandpass. While no ion tail structure is evident by eye in our OH image, we were nonetheless concerned about possible ion contamination that was not accounted for in the standard comet filter reduction procedures.

In order to understand the extent to which our “pure” OH image might be contaminated by improperly removed continuum and/or ions, we extracted radial profiles from the uncalibrated CO^+ , BC, and OH images after removing the background. The radial profiles were binned in distance from the nucleus, ρ , and in azimuthal angle, with a resistant mean used to screen out anomalously high or low pixel values. The dust and ion tails were oriented nearly due east, at a position angle (PA) of $\sim 90^\circ$, slightly offset from the anti-sunward direction of $PA = 79^\circ$, so we determined radial profiles for the sunward and tailward hemispheres as well as 90° wedges centered at 0° , 90° , 180° , and 270° . We then fit slopes to the profiles from $\rho = 4000 - 60000$ km (the inner radius was set to be about twice the seeing disk). The exact slopes retrieved are very sensitive to the background level, but the behavior of slopes with azimuth is not. The OH slope was the flattest, falling off as roughly $\rho^{-0.7}$ in all four quadrants. The BC slope was steeper, falling as roughly $\rho^{-1.1}$ in all four quadrants. The CO^+ exhibited the steepest slope and was the only one that varied significantly with PA, falling as $\rho^{-1.4}$ in the sunward quadrant, and $\rho^{-1.0}$ in the other quadrants. The CO^+ slopes are consistent with the expected behavior of ions whose sunward extent is minimal, while the consistency of the OH and BC slopes at all PAs suggest that each is relatively free of ion contamination. Furthermore, the more rapid fall off of BC and CO^+

compared to OH suggests that, even if there were problems with improper decontamination of the OH image, the flux should increasingly approach the true OH signal at larger distances, with the sunward direction providing the least contaminated OH signal.

This exercise also demonstrated that despite our previous concern about the low signal-to-noise of individual pixels in the OH image, with appropriate binning, clear signal could be detected to at least $\rho = 1.2 \times 10^5$ km. Thus, we measured a radial profile in the sunward quadrant for the “pure” OH image and used this to determine the H_2O production rate on the assumption that the coma was spherically symmetric as follows. We created a synthetic OH profile using J. Parker and M. Festou’s online version¹ of the vectorial model (Festou 1981) using standard parameters given in Table 2 and scaling for the geometry of R2 PanSTARRS during our observations. We then interpolated the model to the midpoints of our radial profile ρ bins and scaled it up or down to minimize χ^2 from $\rho = 4000 - 1.2 \times 10^5$ km. We repeated the process but added a second parameter, a fixed background offset that was allowed to be positive or negative, to minimize χ^2 again. We continued to add complexity by including the BC and CO^+ profiles, first individually and then together, ultimately testing all combinations of vectorial model, fixed background, BC profile, and CO^+ profile. We repeated the fitting using an OH image that was flux calibrated with the continuum component set to zero as a further test of the reduction process.

For the DCT imaging, the best-fit using all parameters is a water production rate, $Q(\text{H}_2\text{O})$, of $\sim 3 \times 10^{26}$ mol/s. The best-fit for the BC scale factor was close to the solar color, implying that the dust was properly removed in the standard processing despite our earlier concerns. Similarly, the best-fits for both images required a CO^+ component, supporting our suspicion that there was some ion contamination. In all cases, the fits yielded $Q(\text{H}_2\text{O})$ between 1 and 5×10^{26} mol/s, with the largest variations occurring for fits using only background fluxes (e.g., no continuum or ion component). We tested reasonable deviations from the standard vectorial model assumptions, such as varying lifetimes and velocities, but these only changed $Q(\text{H}_2\text{O})$ at the $\sim 20\%$ level or less. The fits consistently show that the OH signal is much stronger than the CO^+ and dust continuum beyond $\sim 20,000$ km. Figure 7 shows a “pure” OH image using our best-fit parameters (top left panel), the residual flux after removing the modeled OH component from the “pure” OH image (top right), and the radial profiles in our best-fit model (bottom).

The residual OH image has been highly stretched to emphasize subtle features, but shows a hint of over-removal in the tailward direction and slight under-removal of the inner core. Despite the large number of uncertainties and assumptions needed to deal with this unusual comet, we are confident that we have constrained $Q(\text{H}_2\text{O})$ to less than 10^{27} mol/s with a most likely value of $\sim (3.1 \pm 0.2) \times 10^{26}$ mol/s (Table 3). The uncertainty quoted is strictly for our modeled assumptions and does not include systematic uncertainties that are difficult to quantify but could be larger.

Using the observed flux in the BC image we calculated $Af\rho$ as described in Section 3.3, although for the DCT data we used a smaller photometric aperture projected at the comet of 10,000 km, in line with the typical apertures employed by other optical dust photometry observations. We obtain $Af\rho = 561 \pm 6$ cm (Table 3).

3.5. APO-ARCES

Spectra were extracted and calibrated using IRAF scripts that perform bias subtraction, cosmic ray removal, flat fielding, and wavelength calibration. We removed telluric absorption features, the reflected solar continuum from the dust coma, and flux calibrated the spectra employing our standard star observations. We assumed an exponential extinction law and extinction coefficients for APO when flux calibrating the cometary spectra (Hogg et al. 2001). More details of our reduction procedures can be found in McKay et al. (2012) and Cochran and Cochran (2002). We determined slit losses for the flux standard star observations by performing aperture photometry on the slit viewer images as described in McKay et al. (2014). Slit losses introduce a systematic error in the flux calibration of $\sim 10\%$.

In our optical spectra we report analysis of five molecular species (N_2^+ , CO^+ , CN, NH_2 , C_2) and one atomic species (OI). Our analysis of CN, C_2 , and NH_2 employs the same empirical fitting model employed by McKay et al. (2014), which utilizes a molecular line list from Cochran and Cochran (2002) to fit Gaussian profiles to observed emission features. For N_2^+ and CO^+ we adapt the model from McKay et al. (2014) to include CO^+ by adding line positions from Kuo et al. (1986); Haridass et al. (1992, 2000) and N_2^+ line positions from Dick (1978). We integrate over the fits to measure the observed flux. While we detect multiple bands of CO^+ , we use the (2,0) band for analysis as it has the highest SNR.

¹ <http://www.boulder.swri.edu/wvm-2011/>

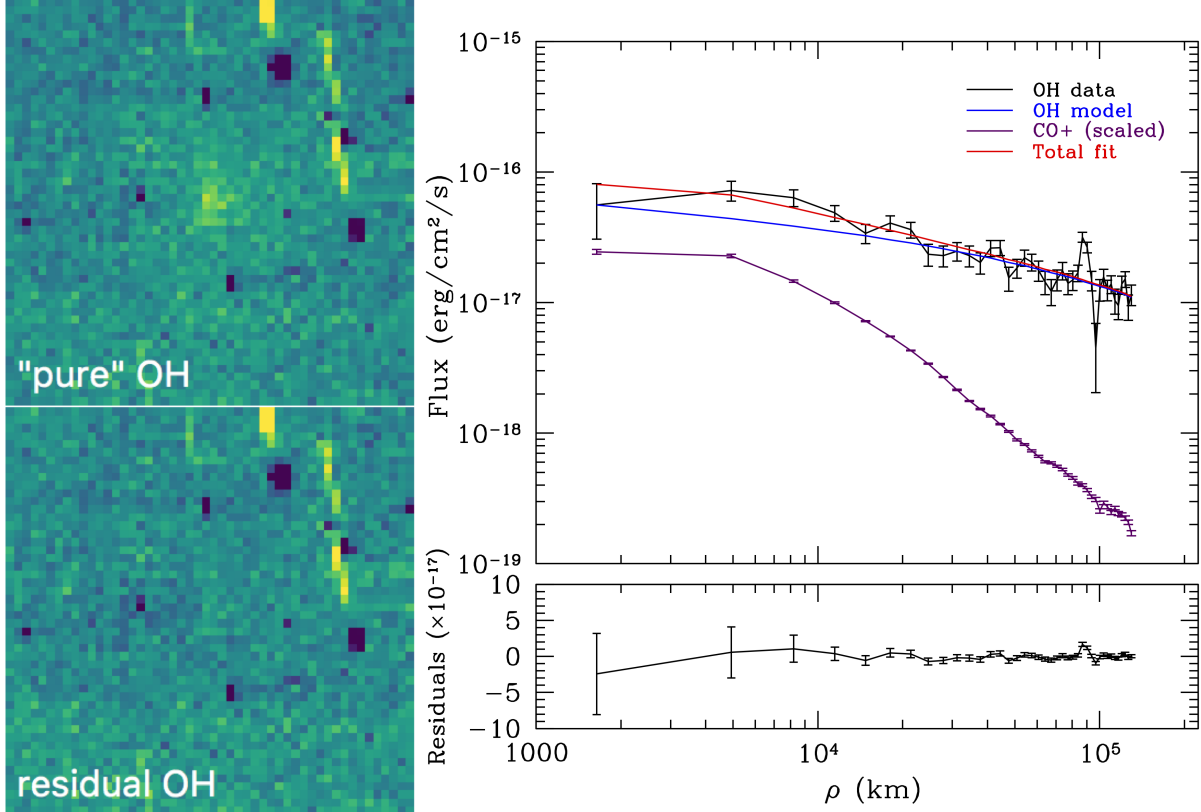


Figure 7. “Pure” OH image produced using the scaling from our best-fit model (top left), residual OH after removing the modeled OH component from the “pure” OH image (top right), and the radial profiles in our best-fit model (bottom). The top panels are zoomed in from the OH image shown in Figure 6, but have the same 8×8 binning applied. They are each $\sim 260,000$ km across at the comet, extending just wider than we fit the radial profiles shown in the bottom panel.

For CN, C₂, and NH₂ these fluxes are converted to production rates using a Haser model in which the input scale lengths are modified to emulate the vectorial model and g-factors from the literature. Molecular lifetimes and g-factors employed are given in Table 2. For [O I], we employ the observed [O I]6300 Å emission as a proxy for H₂O production using a similar Haser model (see McKay et al. (2012, 2014) for more details about the Haser models employed). While [O I]6300 Å emission is often used as a proxy for H₂O production in comets, (e.g. Morgenthaler et al. 2001; Fink 2009; McKay et al. 2018), it assumes that H₂O is the dominant oxygen-bearing species in the coma, which is not the case for R2 PanSTARRS (see Table 3).

Ions do not follow a Haser profile. Therefore we do not calculate production rates from derived fluxes for N₂⁺ and CO⁺, only the relative ratio of N₂⁺/CO⁺ using

$$\frac{N_{N_2^+}}{N_{CO^+}} = \frac{F_{N_2^+} g_{CO^+}}{F_{CO^+} g_{N_2^+}} \quad (4)$$

where N_x denotes column density of species x , F_x is the observed flux of species x , and g_x is the g-factor for the observed transition of species x . The g-factors employed are $g_{CO^+} = 3.55 \times 10^{-3}$ photons s⁻¹ mol⁻¹ (Magnani and A’Hearn 1986) and $g_{N_2^+} = 7.00 \times 10^{-2}$ photons s⁻¹ mol⁻¹ (Lutz et al. 1993).

For the ARCES observations, we show our detections of N₂⁺ and CO⁺ in Fig. 8 and the detection of [O I]6300 Å and [O I]5577 Å emission in Fig. 9. We do not detect CN or NH₂ emission and have a tentative detection of the C₂ bandhead at 5165 Å, all of which we show in Fig. 10.

To derive upper limits on production rates, we employ empirical spectral fits of comet C/2009 P1 (Garradd) at a similar heliocentric distance using the spectral fitting model of McKay et al. (2014) and scale these models so that the strongest lines would be present at the 3σ level (for C₂ we scaled the model so that it corresponded to the

Table 2.
Parameter Values for Optical Species

Molecule	Parent Lifetime (s) ^a	Daughter Lifetime (s) ^a	g-factor (ergs s ⁻¹ molecule ⁻¹) ^a
CN	1.3×10^4	2.1×10^5	2.6×10^{-13}
C2	2.2×10^4	6.6×10^4	4.5×10^{-13}
NH ₂	4.1×10^3	6.2×10^4	6.40×10^{-15}
O I ^b	8.3×10^4	-	-
O I ^c	1.3×10^5	-	-
OH	8.3×10^4	1.3×10^5	1.54×10^{-15}

^a Given for $r=1$ AU. For CN and OH, given for $\dot{r}=0$ km s⁻¹, but varies with \dot{r} .

^b For [O I] from dissociation of H₂O into H₂ and O; branching ratio employed is 0.07 (Bhardwaj and Raghuram 2012)

^c For [O I] from dissociation of OH; branching ratio for H₂O to OH + H employed is 0.855 (Huebner et al. 1992) and the branching ratio for OH to O + H is 0.094 (Bhardwaj and Raghuram 2012).

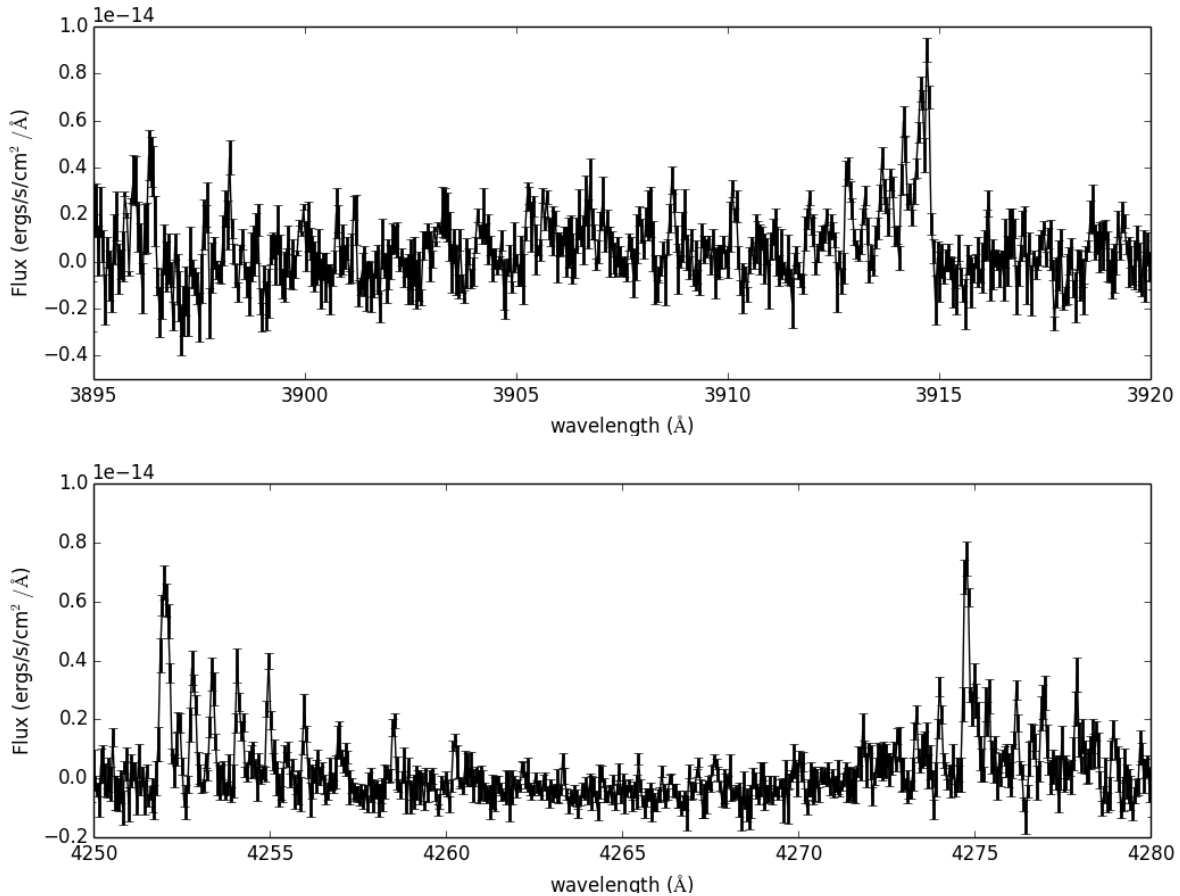


Figure 8. Spectra showing the N₂⁺ (0-0) band (top) and CO⁺ (2-0) band (bottom) in R2 PanSTARRS. The derived N₂/CO ratio is 0.05 ± 0.01 , in agreement with other measurements by Cochran and McKay (2018), Biver et al. (2018), and Opitom et al. (2019).

candidate bandhead feature). We then integrated over this model to obtain an upper limit on the observed flux and convert to production rate using our Haser model as described above. We present the production rate upper limits for CN, NH₂, and C₂ in Table 3. Regardless of whether the inferred flux for C₂ is interpreted as an upper limit or a detection, the upper limit inferred for C₂H₂ is unchanged since C₂ has multiple sources in cometary comae (Combi

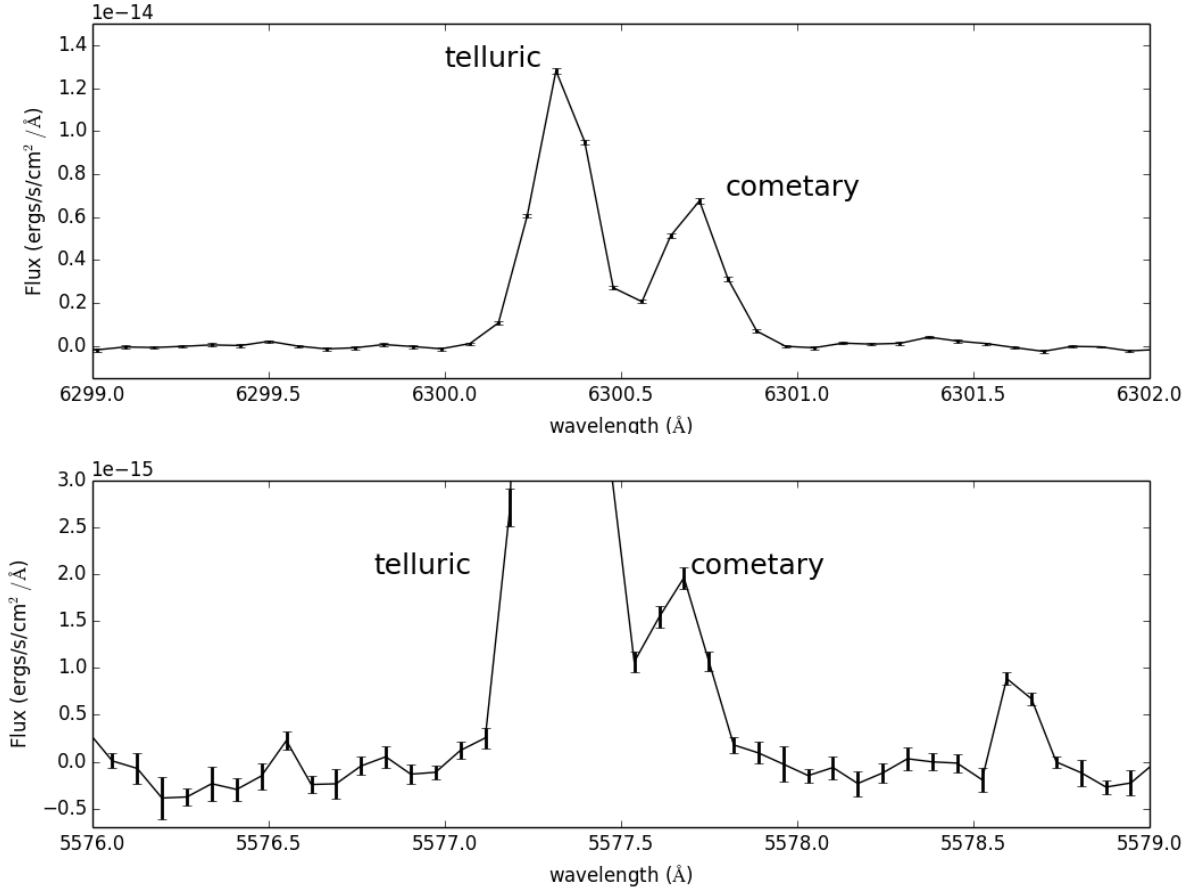


Figure 9. The [O I]6300 Å (top) and [O I]5577 Å (bottom) lines in comet R2 PanSTARRS. The telluric line is blueward of the cometary feature. While often used as a proxy for H₂O production in comets, the large abundances of CO and CO₂ in R2 PanSTARRS make the derived water production rates an overestimate. This conclusion is supported by the disagreement between the derived water production rates from the [O I]6300 Å line and our OH observations. Therefore we do not consider the [O I]6300 Å line as a robust proxy for H₂O production in R2 PanSTARRS.

and Fink 1997). For ARCES observations we compare to the iSHELL observations of CO because the data were taken contemporaneously and both are narrow slit spectrometers sampling similar portions of the coma.

From the ARCES spectra, we measure an N_2^+ / CO^+ ratio of 0.05 ± 0.01 . We follow the arguments of Cochran and McKay (2018) and assume that $N_2^+ / CO^+ = N_2 / CO$ (see Section 4 for discussion of the validity of this assumption). Therefore we infer an N_2 / CO ratio of 0.05 ± 0.01 . Using the CO production rate derived from our iSHELL observations, we derive an N_2 production rate of 4.8×10^{27} mol s⁻¹ (see Table 3).

We present the H₂O production rates derived from the [O I]6300 Å emission measured by ARCES and OH emission from DCT in Table 3. There is a clear discrepancy (factor of ~ 30) between the H₂O production rate derived from the [O I]6300 Å emission and the value derived from our OH narrowband observations. However, the methodology for deriving water production rates from [O I]6300 Å emission assumes that H₂O photodissociation is the dominant source of O I in the coma. While this is a valid assumption for most comets and has been used in the past to derive reliable H₂O production rates (e.g., Morgenthaler et al. 2001; Fink 2009; McKay et al. 2018), the large CO and CO₂ production rates found both by ourselves and other authors compared to our derived water production rate suggest this is not a valid assumption for R2 PanSTARRS. Not accounting for contributions from the photodissociation of other oxygen-bearing species such as CO and CO₂ when they are more abundant than H₂O results in a large overestimate of the water production rate, which is what we observe when comparing to the production rate derived from our OH observations. As OH release into the coma is always dominated by H₂O, it is a more reliable proxy for H₂O production than [O I]. Therefore we adopt the value of Q_{H_2O} inferred from our OH observations as a more accurate measure of the H₂O production rate.

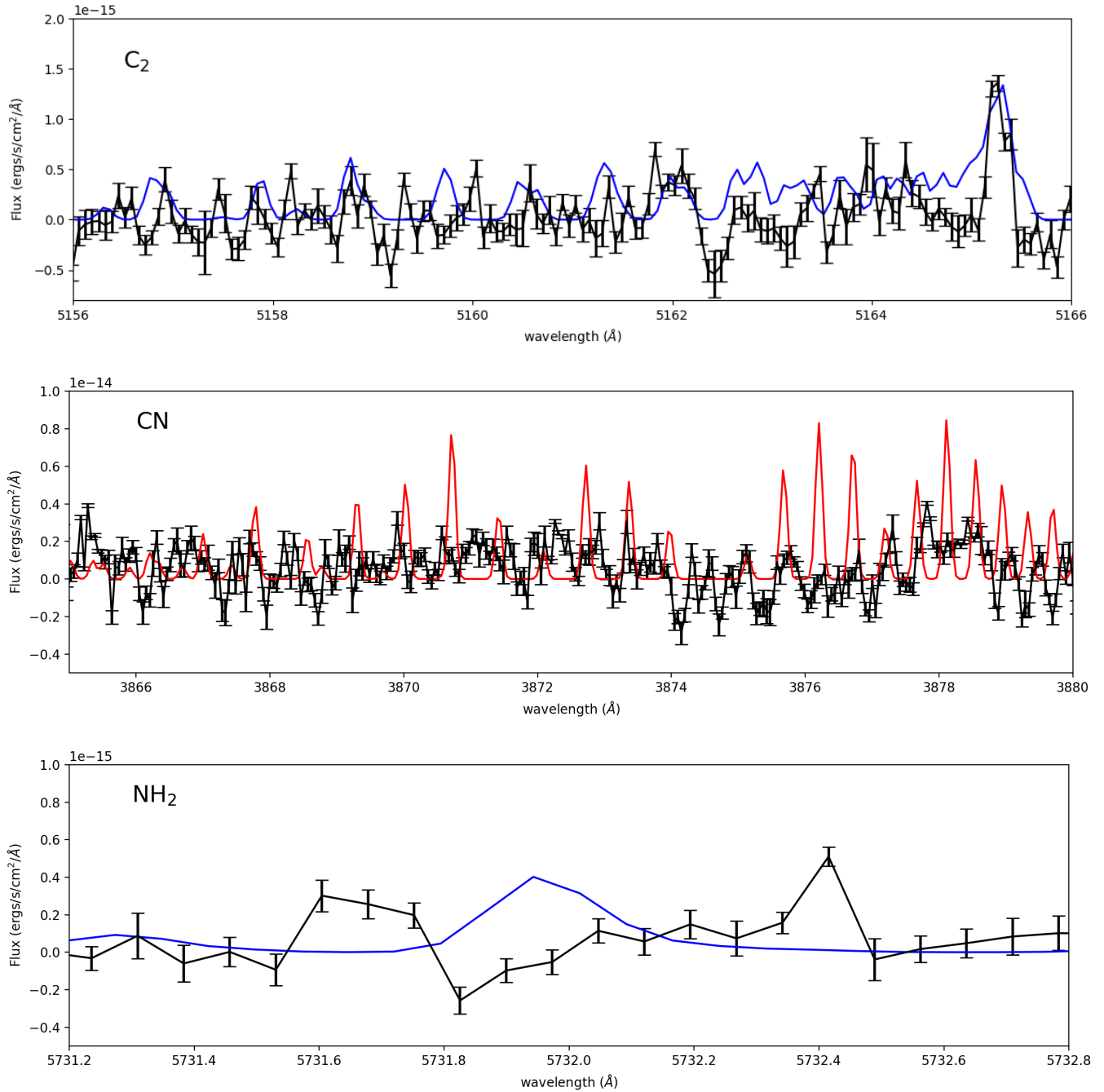


Figure 10. Spectral regions around C_2 (top), CN (middle), and NH_2 (bottom) emission features. The number above the top corner of each plot (e.g. “ $1e-15$ ” for C_2) denotes the multiplier for the units of the y-axis. CN and NH_2 are not detected, while there is a candidate feature corresponding to the C_2 bandhead. Overplotted are empirical fits to a spectrum of C/2009 P1 (Garradd) at similar heliocentric distance scaled to the flux levels of the observed R2 PanSTARRS spectra, which serve as 3σ upper limits on the observed flux. For C_2 the model matches the peak flux of the candidate bandhead at 5165 Å. Although we interpret this as a tentative detection of C_2 , for this work we are employing C_2 as a constraint on the C_2H_2 abundance, so even a detection of C_2 only provides an upper limit on C_2H_2 due to multiple sources of the C_2 molecule in comets. These upper limits then provide us with an upper limit on the production rate.

The O I photochemistry in comets has been of interest for some time (e.g., Festou and Feldman 1981; Cochran 2008; McKay et al. 2013, 2015; Decock et al. 2013, 2015), and the study of both the [O I]6300 Å line as well as

the [O I]5577 Å line (which we also detect in our ARCES spectra, see Fig. 9) in such a CO and CO₂-rich comet could provide new insights into O I photochemistry in comets. We measure the flux ratio of the [O I]5577 Å line to the sum of the [O I]6300 Å and [O I]6364 Å lines (the oxygen line ratio) to be 0.20 ± 0.03 , in agreement with the value of 0.23 ± 0.03 measured by [Opitom et al. \(2019\)](#). This ratio is higher than typically observed but is similar to other comets observed at heliocentric distances near 3 AU ([McKay et al. 2012](#); [Decock et al. 2013](#); [McKay et al. 2015](#)). This is consistent with the large CO₂/H₂O and CO/H₂O ratios observed. However, a detailed study of the O I photochemistry in R2 PanSTARRS is beyond the scope of this paper and will be pursued in a future publication.

3.6. Summary of Production Rates and Relative Abundances

A summary of our resulting production rates and abundances is presented in Table 3. We pursued several methods for determining the water production rate: H₂O and OH prompt emission from iSHELL, OH emission from DCT, and [OI]6300 emission from APO ARCES. The OH data from DCT provided the best measure of H₂O production and therefore all mixing ratios compared to H₂O use the DCT-derived Q(H₂O) as the reference. While we detected [O I]6300 emission there is significant evidence that this emission is actually dominated by contributions from CO₂ and/or CO photodissociation rather than H₂O, and so for R2 PanSTARRS it does not serve as a reliable proxy for H₂O (see Section 3.5).

Table 3. Production Rates and Abundances

Instrument	Species	Q (10 ²⁷ mol s ⁻¹)	X/H ₂ O ^a (%)	X/CO ^b (%)
IRTF-iSHELL	CO	95.4 ± 9.1	(3.08 ± 0.35) × 10 ⁴	-
	CH ₄	0.56 ± 0.07	181 ± 25	0.59 ± 0.09
	OCS	< 0.23	< 74	< 0.24
	C ₂ H ₆	< 0.085	< 27	< 0.089
	CH ₃ OH	< 0.36	< 116	< 0.38
	H ₂ CO	< 0.49	< 158	< 0.51
	H ₂ O ^c	< 78.4	-	< 82
	H ₂ O ^d	< 72.9	-	< 76
<i>Spitzer</i> IRAC	CO ₂ ^e	10.0 ± 1.0	3230 ± 380	18.2 ± 3.5
	Afρ	890 ± 19 cm	-23.54 ± 0.03 ^f	-25.79 ± 0.04 ^g
ARO-SMT	CO	55.0 ± 8.9	(1.77 ± 0.31) × 10 ⁴	-
APO-ARCES	N ₂	4.8 ± 1.1 ^h	1550 ± 370	5.0 ± 1.0
	CN	< 0.02	< 6.5	< 0.021
	NH ₂	< 0.01	< 3.2	< 0.010
	C ₂	< 0.021	< 6.8	< 0.022
	H ₂ O (via [O I])	10.5 ± 0.5	-	11.0 ± 1.2
DCT-LMI	H ₂ O (via OH)	0.31 ± 0.02	-	0.32 ± 0.04
	Afρ	561 ± 6 cm	-23.74 ± 0.03 ^f	-25.99 ± 0.04 ^g

^a Compared to the measured value from OH observations with the DCT, as this is the most robust measure of the H₂O production rate.

^b Compared to the iSHELL CO production rate except for CO₂ and Afρ, which is compared to the SMT CO value as this value was measured contemporaneously and was used to correct the *Spitzer* observations for the expected CO contribution. N₂/CO is calculated from the optical observations of N₂⁺ and CO⁺ as described in the text.

^c Derived from H₂O lines in the M2 setting.

^d Derived from OH prompt emission in the Lp1 setting.

^e Derived accounting for the expected CO contribution based on the SMT observations using the methodology detailed in Section 3.3.

^f $\log(Af\rho/Q_{H_2O})$

^g $\log(Af\rho/Q_{CO})$

^h Calculated using the N₂/CO ratio derived from optical observations multiplied by the iSHELL CO production rate.

3.7. *Active Areas*

We employ our CO₂, H₂O, and CO production rates to calculate the active areas of the cometary surface using the sublimation model of Cowan and A'Hearn (1979), which are given in Table 4. Following arguments given in Bodewits et al. (2014), McKay et al. (2017), and McKay et al. (2018), we adopt the slow rotator model, for which every facet of the nucleus surface is in equilibrium with the solar radiation incident upon it. While the size of the nucleus of R2 PanSTARRS is not known, we convert these active areas to active fractions for a 1 km and 10 km radius nucleus, which encompasses the range of most cometary nuclei for which measurements are available, including an upper limit of $R < 15$ km determined for R2 PanSTARRS from Wierchos and Womack (2018).

Table 4. Active Areas and Active Fractions

Species	Vaporization Rate (10 ¹⁶ mol s ⁻¹ cm ⁻²)	Production Rate (10 ²⁷ mol s ⁻¹)	Active Area (10 ¹⁰ cm ²)	Active Fraction (r=1 km, %)	Active Fraction (r=10 km, %)
CO	30.0	95.4 ± 9.1 ^a	31.8 ± 3.0	252 ± 24	2.52 ± 0.24
CO	30.0	55.0 ± 9.0 ^b	18.3 ± 3.0	145 ± 24	1.45 ± 0.24
CO ₂	8.22	10.0 ± 1.0	12.0 ± 1.2	96 ± 10	0.96 ± 0.10
H ₂ O	2.00	0.31 ± 0.02	1.6 ± 0.1	12.2 ± 0.8	0.122 ± 0.008

^a iSHELL-derived CO production rate

^b SMT-derived CO production rate

4. DISCUSSION

4.1. *Other Potential Molecular Emissions in Spitzer Imaging*

As our CO₂ abundance is dependent on an analysis of broadband imaging, not spectroscopy, it is possible there are other emission features in our bandpass besides CO₂ and CO, the species commonly assumed to dominate the flux. This would lead to an overestimate of the CO₂ production rate. The leading neutral candidates are OCS and N₂O. Hot bands of water in the 4.5-5.0 μ m region would normally be important (Ootsubo et al. 2012) but the extremely low H₂O/CO and H₂O/CO₂ ratios for R2 PanSTARRS mean they can be neglected.

OCS has a strong band at ~ 4.9 μ m, and has been observed in comets at an abundance of approximately 0.1-0.4% with respect to H₂O (Bockelée-Morvan et al. 2004; Mumma and Charnley 2011; Dello Russo et al. 2016b, and references therein). OCS is covered by the M2 grating setting in our iSHELL observations (Fig. 1), and was not detected, placing an upper limit on its abundance ratio compared to CO of 0.24%. At this level OCS is not a significant contributor to the 4.5 μ m band flux.

The other neutral molecule with strong emissions in the 4.5 μ m bandpass is N₂O. To date, N₂O has never been detected in a comet, despite ISO and AKARI observations that cover this wavelength range (Crovisier et al. 1997; Ootsubo et al. 2012). As of this writing we are not aware of any reported detection of N₂O by the Rosetta instruments around 67P/Churyumov-Gerasimenko. However, the large N₂ abundance and the presence of an intrinsically strong N₂O band at ~ 4.5 μ m could perhaps indicate a strong contribution of this molecule to our *Spitzer* photometry. The N₂O emission is too far to the blue to be covered by our iSHELL observations in the M2 grating, and also the region around the N₂O emission band is heavily affected by telluric CO₂ absorption. Therefore we cannot definitively rule out the presence of N₂O emission in our *Spitzer* images. The g-factor for the relevant N₂O transition is 1.5×10^{-3} photons/s/mol, meaning that an N₂O production rate of $\sim 1.8 \times 10^{28}$ mol/s could account for the residual flux we attribute to CO₂. This suggests that even at $\sim 1.8 \times 10^{27}$ mol/s N₂O could account for 10% of the flux we attribute to CO₂. However, N₂O is also very efficient at releasing O(¹S) into the coma (Huebner et al. 1992), and at these high production rates we may expect it to dominate the O I photochemistry and drive the oxygen line ratio to be ~ 1 . However, we measure an oxygen line ratio of 0.20 (Section 3.5), suggesting that N₂O is not a dominant source of O I in the coma. While O I photochemistry in comets is not well understood, this, combined with a lack of previous detections in comets, likely implies that N₂O is not contributing much more than 10% to the residual flux we attribute to CO₂.

Lastly, the $\Delta v=1-0$ band of CO⁺ is located at ~ 4.6 μ m. We do indeed observe a faint tail feature with structures reminiscent of an ion tail in both *Spitzer* epochs (Fig. 5). We attribute this to the CO⁺ band based on the large CO

production rate and the strong CO^+ tails observed in the optical for R2 PanSTARRS. However, this tail is much fainter than the neutral emission and only appears obvious in Figure 5 due to the image enhancement process. Additionally, this band is covered by our iSHELL observations yet is not detected. Therefore we conclude that CO^+ cannot account for the observed excess emission that we attribute to CO_2 .

While we cannot unequivocally rule out N_2O emission, we conclude that our *Spitzer* 4.5 μm band imaging is most likely dominated by a combination of CO_2 and CO emission. After accounting for the expected CO contribution based on independent observations with other facilities, we think that our analysis provides an accurate measure of the CO_2 abundance in R2 PanSTARRS.

4.2. Comparison to Other Observations of R2 PanSTARRS

Our N_2/CO ratio agrees well with the measurements made by Cochran and McKay (2018) in December 2017, almost two months before our observations, as well as measurements by Biver et al. (2018) made about a week before our observations and measurements by Opitom et al. (2019) about two weeks after our observations. This suggests there was little evolution in the N_2/CO ratio over the December 2017-February 2018 time frame.

Our iSHELL CO production rate agrees well with values determined by de Val-Borro et al. (2018) and Biver et al. (2018), whose observations were 1-2 weeks before ours (although these works used an asymmetric outgassing model while we assume symmetric outflow). Our value is higher than that found by Wierzchos and Womack (2018) using the SMT in late December 2017 and mid-January 2018, as well as the value we measure from our SMT observations. This could be due to different FOV or the narrow nature of our slit. There is evidence from the millimeter observations of Biver et al. (2018) and Wierzchos and Womack (2018) that there is a significant sunward outgassing component, an enhancement also observed in our *Spitzer* imaging (see Fig. 5). As the iSHELL slit was oriented along the Sun-comet line, we may have sampled this enhancement, which coupled with our application of a symmetric outgassing model may result in an overestimate of the CO production rate, but we do not observe a strong asymmetry in the CO line profile (see Section 3.1, Fig. 3), meaning the iSHELL observations were not sensitive to the asymmetry inferred from the mm and *Spitzer* observations. One reason for this discrepancy could be the limited spatial coverage of the iSHELL slit (slit width $0.75'' \times$ length $\sim 6''$) compared to the much larger circular beams in the sub-mm (10-30'') and the arcminute spatial scale covered by the *Spitzer* imaging. A narrow feature that is only slightly offset from the solar direction could be missed by the narrow iSHELL slit, while still revealing an asymmetry that would be evident only on larger spatial scales. There is evidence from the coma morphology in the *Spitzer* images that the asymmetry manifests as a large fan-shaped feature (Fig. 5, rightmost column), perhaps implying the asymmetry would not be as pronounced in the inner coma sampled by iSHELL.

In analyzing our iSHELL spectra we adopt the gas expansion velocity (v_{exp}) measured by SMT (0.52 km/s), but as the iSHELL slit samples the very inner coma, it is possible the gas may not have been fully accelerated to the speed observed at larger nucleocentric distances. A $\sim 30\%$ smaller assumed v_{exp} (i.e., from 0.52 km/s to 0.35-0.40 km/s) would bring the iSHELL and SMT results for Q_{CO} into agreement within their respective $1-\sigma$ uncertainties. As the resolving power of our iSHELL spectra ($\lambda/\Delta\lambda \sim 4 \times 10^4$) is insufficient to resolve the cometary lines, we obtain no information regarding v_{exp} and therefore we cannot confirm or refute the possibility of a lower expansion velocity in the inner coma. However, the rotational temperature we measured for CO (13 ± 2 K) is significantly lower than that obtained for CH_3OH from IRAM of 23K (Biver et al. 2018). This discrepancy may be due to photolytic heating of the coma as the gas expands. Based on this result we might expect a smaller expansion velocity to be more relevant to the iSHELL observations since the terminal region spanned lines-of-sight offset only $\sim 1-5''$ from the nucleus, in contrast to the much larger SMT/IRAM beam sizes ($\sim 10-30''$). In any case, while absolute production rates are proportional to v_{exp} (assuming the beam size is small compared to the photodissociation scale length, which is the case for all species reported here), relative abundances (i.e., mixing ratios) are relatively insensitive to the adopted value of v_{exp} as long as a common v_{exp} is assumed for all species, which is the case in this work. Therefore, we would expect negligible changes in abundance ratios for the other species included in the M2 and Lp1 settings (e.g., Table 3).

The different rotational temperature measured from our iSHELL observations versus the IRAM observations of Biver et al. (2018) and adopted for our SMT analysis could affect our results. For the iSHELL observations adopting $T_{rot}=23\text{K}$ results in a $\sim 10\%$ higher CO production rate, while adopting $T_{rot}=13\text{K}$ for the SMT observations results in a CO production rate $\sim 30\%$ higher than the value for $T_{rot}=23\text{K}$. Adopting the higher T_{rot} for the iSHELL data results in a $\sim 70\%$ larger CH_4 production rate, 15-20% less sensitive upper limits on CH_3OH and C_2H_6 , a 15% more sensitive upper limit on H_2CO , and a 10% more sensitive upper limit on OCS . In terms of mixing ratios compared to

CO, the CH₄/CO ratio is most affected, having a value 50% higher for $T_{rot}=23\text{K}$ than for $T_{rot}=13\text{K}$. The upper limits on C₂H₆/CO and CH₃OH/CO change minimally ($\sim 5\%$) for the different value of T_{rot} , while the upper limits on H₂CO/CO and OCS/CO are approximately 20% more sensitive for $T_{rot}=23\text{K}$. Analysis for the other instruments does not depend on T_{rot} , though the slightly higher CO production rates determined from both iSHELL and SMT data using the alternate rotational temperature would result in proportionately lower values of the mixing ratios compared to CO.

Our upper limit for CH₃OH is a factor of three lower than the detection by Biver et al. (2018) (this is independent of the value of T_{rot} , as are all the comparisons in this paragraph), which could be due to temporal and/or spatial variability in CH₃OH outgassing. The different projected areas observed for the IRAM and iSHELL observations could account for this discrepancy if a fraction of CH₃OH is released as icy grains in the coma. At the same time, our H₂CO upper limit is consistent with the detection of Biver et al. (2018). Our HCN upper limit (inferred from CN) is consistent with both the upper limit found by Wierzchos and Womack (2018) and the detection reported by Biver et al. (2018). Our H₂O production rate inferred from the OH DCT data is consistent with the upper limits reported by Biver et al. (2018) from observations of the OH 18 cm line at Nancay and by Opitom et al. (2019) using narrowband photometry from the TRAPPIST telescope.

At the time of this writing our results are the first reported detections or upper limits on CO₂, CH₄, C₂H₆, C₂H₂, OCS, and NH₃ in R2 PanSTARRS. While Opitom et al. (2019) report a lower limit on the N₂⁺/NH₂ ratio (a proxy for N₂/NH₃), this is a lower limit on the column density ratio in the slit, and because of the different spatial distributions of ions and neutrals, interpreting the column density ratio as an actual abundance ratio is complicated. Assuming N₂⁺/CO⁺=N₂/CO, we have used our neutral CO measurements to convert the N₂⁺/CO⁺ to an equivalent N₂ production rate, which then can be compared to the production rates derived for other neutrals such as NH₃ and HCN, as was also done by Wierzchos and Womack (2018). With those caveats aside, the lower limit on N₂/NH₃ provided by Opitom et al. (2019) is consistent with our constraints.

Opitom et al. (2019) also detected CO₂⁺ emission and derive a CO₂⁺/CO⁺ ratio of 1.1 ± 0.3 . They do not interpret this as the CO₂/CO ratio, as CO₂ can also contribute to observed CO⁺ emission. For this reason Opitom et al. (2019) also express caution when interpreting the N₂⁺/CO⁺ ratio as a direct measurement of N₂/CO, as CO₂ photodissociation could contribute to the observed CO⁺ emission and therefore the measured N₂⁺/CO⁺ ratio actually only provides a lower limit on N₂/CO. However, from our *Spitzer* observations of neutral CO₂, we derive CO₂/CO $\sim 18\%$, and at this low abundance CO photoionization should be the dominant source of CO⁺ ions (Huebner et al. 1992). This appears to disagree with the large CO₂⁺/CO⁺ ratio observed by Opitom et al. (2019). The reason for the discrepancy between ion and neutral observations is unknown, but may be related to our understanding of CO₂ and CO photochemistry.

The $Af\rho$ value we find for R2 PanSTARRS from our DCT BC imaging is lower than other measurements by Opitom et al. (2019) as well as from the cometary database developed by T. Noel² quoted by Biver et al. (2018). There is some evidence for temporal variability in the observations of Opitom et al. (2019), so that may explain some of the discrepancy. Variable gas contamination by strong CO⁺ emission could also be present, especially for the broadband photometry quoted by Biver et al. (2018). The $Af\rho$ value derived from our *Spitzer* imaging is higher than all values reported in the optical, including our DCT observations, which were contemporaneous with the *Spitzer* epoch on UT February 21. However, the different wavelength regimes for the IR and optical data make it unclear how comparable the $Af\rho$ values actually are. For the *Spitzer* data, we employed a larger photometric aperture than the optical studies (28,000 km vs. 10,000 km); using a smaller aperture in line with other studies yields $Af\rho \sim 1000$ cm, larger than found for the original aperture. While $Af\rho$ is independent of aperture size for ideal comae, the presence of a dust tail and acceleration of the dust can account for the decreasing trend with aperture size we observe for $Af\rho$. Spectral reddening of light scattered by comae can vary with wavelength, especially over such a large spectral range (Jewitt and Meech 1986). Nevertheless, we calculate the effective BC (0.45 μm) to 3.6 μm spectral slope as $\sim 1.8\%$ per 100 nm, similar to other comets observed in the NIR by Jewitt and Meech (1986).

4.3. Comparison to Other Comets

In this section we compare R2 PanSTARRS to other comets. First we compare to the cometary population as a whole, then specifically to other comets observed at similar heliocentric distance.

² <http://www.lesia.obspm.fr/comets/>

4.3.1. *Cometary Population*

Table 5 summarizes derived production rates (or upper limits) for R2 PanSTARRS, along with mixing ratios relative to H₂O and CO, for 12 species. For comparison, the average values of these mixing ratios for the sample of Oort Cloud Comets observed to date are also presented. Most values for R2 PanSTARRS are from this work, though for CH₃OH, HCN, and H₂CO our observations only provide upper limits while Biver et al. (2018) secured detections, so in Table 5 we present the detected production rates for these species from Biver et al. (2018).

All detected species in R2 PanSTARRS are heavily enriched compared to H₂O. CO is enriched by four orders of magnitude with N₂ enriched by a similar amount (though the small sample size of N₂ measurements in comets makes this difficult to quantify), while CH₄, CH₃OH, and CO₂ are enriched by a factor of ~ 160 -200. H₂CO and HCN have less drastic enrichments of ~ 40 and 6, respectively, though these are still extraordinary enhancements never before observed in a comet. We cannot draw any conclusions regarding the abundances of C₂H₆, NH₃, C₂H₂, or OCS compared to H₂O, though our results imply that while they could be heavily enriched compared to H₂O, this enrichment is not as drastic as inferred for species such as CO, and may be more in line with that observed for species such as H₂CO or HCN.

While a definitive comparison to H₂O is not possible for all species, the strong CO detection allows comparison of all species to CO. We find all species searched for are heavily depleted compared to CO, except for N₂ which is enhanced. Even for species that aren't detected, the upper limits are sensitive enough to demonstrate heavy depletions. All depleted species are underabundant by at least 1-3 orders of magnitude compared to other comets.

R2 PanSTARRS has provided a glimpse into a rarely observed (alternative) compositional taxonomy, with CO replacing H₂O as the dominant gas in the coma. The measured abundance ratio CH₄/CO ($\sim 0.6\%$; Table 3) approaches the mean CH₄/H₂O and C₂H₆/H₂O ratios among comets from the Oort cloud (Dello Russo et al. (2016b), Bockelée-Morvan et al. (2004)). In contrast, C₂H₆ is strongly depleted (by a factor of at least 6.6 relative to CH₄), with C₂H₆/CO rivaling or surpassing the level of depletion of C₂H₆ (relative to H₂O) measured for disrupted comet C/1999 S4 (LINEAR), a current “end-member” in terms of its severe depletion in all reported volatiles with the exception of HCN (Mumma et al. 2001). Another peculiarity of R2 PanSTARRS is the large N₂ abundance, with N₂ being the dominant reservoir of volatile nitrogen, more abundant than even H₂O (only CO₂ and CO are more abundant than N₂). Typically NH₃, and to a lesser extent HCN, are the most abundant nitrogen-bearing volatiles in comets. However, in R2 PanSTARRS NH₃/N₂ < 0.21% and HCN/N₂ = $0.08 \pm 0.03\%$. So unless another more complicated form of volatile nitrogen that is not constrained by our observations (e.g., N₂O, C₂N₂, CH₃CN) is present at significant levels, more than 99% of the volatile nitrogen in R2 PanSTARRS is contained in N₂. There are not many measurements of the NH₃/N₂ value in comets; however, this limit for R2 PanSTARRS is much lower than measured for comet Halley ($\sim 1000\%$), and is closer to derived values for several dense molecular clouds in star-forming regions ($\sim 0.6\%$) (Womack et al. 1992). The very low derived relative abundance of NH₃/N₂ is consistent with the suggestion by Wierzbos and Womack (2018) that R2 PanSTARRS formed in an environment with decreased photodissociation of N₂, leading to preserving, or shielding, of N₂ and inhibited production pathways of hydrogen-rich species, such as HCN and NH₃ (Hily-Blant et al. 2017).

We show additional mixing ratios compared to CO₂, CH₄, CH₃OH, H₂CO, and HCN in Table 6, with the mean ratio observed among comets listed in parentheses. A subset of this compilation is shown visually as histograms in Fig. 11. For mixing ratios compared to CO₂ we employ the average CO₂/H₂O ratio in the AKARI sample (Ootsubo et al. 2012), while other species like CH₃OH have their average abundance compared to H₂O derived from ground-based IR studies (Dello Russo et al. 2016b), meaning that CO₂ and the other species were not observed contemporaneously and in most cases the sample of AKARI and ground-based IR observations sampled different comets. This means interpretation of the average CO₂ abundance in Table 6 is limited by the degree to which the AKARI and ground-based IR studies provide a random sample of the cometary population.

Almost all mixing ratios in R2 PanSTARRS deviate from typical values by at least a factor of three, although for some species that were not detected we do not have sufficient sensitivity to rule out a normal abundance (e.g. C₂H₆/HCN). HCN is universally depleted by at least an order of magnitude compared to all detected species except H₂O. Interestingly CH₃OH/CO₂ and CH₃OH/CH₄ are the only mixing ratios that are similar (within a factor of two) to the average values observed among comets. Perhaps this commonality between the peculiar R2 PanSTARRS and other comets can shed light on its origin. In any case, the almost universal peculiarity of the observed abundances in R2 PanSTARRS compared to other comets implies that this is not a case of one or two species being anomalous (e.g., CO being heavily enriched and H₂O being heavily depleted), but a complete composition fundamentally different from

Table 5. Summary of Production Rates and Relative Abundances

Instrument	Species	Q (10^{27} mol s $^{-1}$)	X/H $_2$ O (%)	Mean X/H $_2$ O a (%)	X/CO (%)	Mean X/CO b (%)
<i>Spitzer</i>	CO $_2$	10.0 \pm 1.0	3230 \pm 380	17.0 \pm 6.0	18.2 \pm 3.5	425 \pm 178
IRTF iSHELL	CO	95.4 \pm 9.1	(3.08 \pm 0.35) \times 10 4	4.0 \pm 0.9	-	-
	CH $_4$	0.56 \pm 0.07	181 \pm 25	0.88 \pm 0.10	0.59 \pm 0.09	22.0 \pm 5.5
	C $_2$ H $_6$	< 0.085	< 27	0.63 \pm 0.10	< 0.089	15.8 \pm 4.4
	OCS	< 0.23	< 74	\sim 0.25	< 0.24	\sim 6.3
APO ARCES	N $_2$ c	4.8 \pm 1.1	1550 \pm 370	\ll 1? d	5.0 \pm 1.0	< 1? d
	NH $_3$ e	< 0.01	< 3.2	0.91 \pm 0.30	< 0.010	22.8 \pm 9.1
	C $_2$ H $_2$ f	< 0.021	< 6.8	0.16 \pm 0.03	< 0.022	4.0 \pm 1.2
DCT LMI	H $_2$ O g	0.31 \pm 0.02	-	-	0.32 \pm 0.04	2500 \pm 560
IRAM h	CH $_3$ OH	1.12 \pm 0.07	360 \pm 32	2.21 \pm 0.24	1.04 \pm 0.08	55.3 \pm 13.8
	H $_2$ CO	0.045 \pm 0.007	14.5 \pm 2.4	0.33 \pm 0.08	0.043 \pm 0.006	8.0 \pm 2.6
	HCN	(4.0 \pm 1.0) \times 10 $^{-3}$	1.3 \pm 0.3	0.22 \pm 0.03	(3.8 \pm 1.0) \times 10 $^{-3}$	5.5 \pm 1.4

a Mean mixing ratio compared to H $_2$ O in the sample of Oort Cloud comets observed to date. The uncertainties reflect the standard deviation in measured values. All values except for N $_2$ and CO $_2$ are from [Dello Russo et al. \(2016a\)](#). The CO $_2$ value is from [Ootsubo et al. \(2012\)](#).

b Mean mixing ratio compared to CO in the sample of Oort Cloud comets observed to date. The uncertainties reflect the standard deviation in measured values. References for abundances are the same as for H $_2$ O detailed in footnote a .

c Derived by multiplying the derived N $_2$ /CO ratio from our ARCES observations by the CO production rate determined from our iSHELL observations.

d Due to the lack of observations of N $_2$ in comets, the mean mixing ratios compared to H $_2$ O and CO are not meaningful to calculate. Therefore the number included is based on past observations discussed in [Cochran and McKay \(2018\)](#) and has very large uncertainty (indicated by the “?”).

e Derived from our NH $_2$ upper limit assuming all NH $_2$ is released via NH $_3$ photodissociation (i.e. $Q_{NH_3}=Q_{NH_2}$).

f Derived from our C $_2$ upper limit assuming all C $_2$ is released via C $_2$ photodissociation (i.e. $Q_{C_2}=Q_{C_2H_2}$).

g Derived from our OH narrowband observations.

h Production rates from [Biver et al. \(2018\)](#). Mixing ratios compared to CO are taken directly from [Biver et al. \(2018\)](#), mixing ratios for H $_2$ O are calculated using our derived H $_2$ O production rate.

the ensemble of comets observed to date.

This strong deviation from a “typical” cometary composition is also illustrated in [Fig. 12](#). Over 80% of the volatile composition of R2 PanSTARRS is CO, while H $_2$ O is relegated to the status of a trace volatile. N $_2$ is also much more abundant than in typical comets, and more abundant than the other typical trace species (i.e., other than CO, H $_2$ O, and CO $_2$) combined. CO $_2$ as a fraction of the volatile inventory of R2 PanSTARRS is actually fairly close to typical comets.

R2 PanSTARRS has a much lower $Af\rho$ than other comets with such high gas production observed at similar heliocentric distances, though concluding whether R2 PanSTARRS is dust-rich or gas rich depends on which volatile is used as the reference. The value of $\log[Af\rho/Q(\text{H}_2\text{O})]$ determined for R2 PanSTARRS is larger by a factor of 5-10 than most comets observed at $R_h \sim 3$ AU in the survey by [A’Hearn et al. \(1995\)](#), meaning that when H $_2$ O is the comparison gas R2 PanSTARRS is considered quite dusty. However, $\log[Af\rho/Q(\text{CO}_2)]$ is at the low end of comets observed with *Spitzer* and NEOWISE ([Bauer et al. 2015](#), [Kelley et al. in prep](#)), and approximately a factor of 10 lower than any Oort Cloud comet in those samples. So compared to CO $_2$ R2 PanSTARRS is considered a gas-rich comet. While no systematic study comparing $Af\rho$ to CO has been done, the extremely high CO production rate suggests that if CO is the reference gas, R2 PanSTARRS is incredibly gas-rich, possibly the most gas-rich comet ever observed. Even in terms of the total gas production (typically dominated by H $_2$ O but dominated by CO in the case of R2 PanSTARRS) compared to $Af\rho$, R2 PanSTARRS is very gas-rich.

4.3.2. Comets at Large Heliocentric Distance

A caveat to consider when interpreting observations of R2 PanSTARRS is the fairly large heliocentric distance of the observations, ~ 2.8 AU. We compare to other comets observed at large heliocentric distance (approaching or beyond 3 AU) in [Table 7](#). While these comets do show depletions compared to CO, R2 PanSTARRS shows heavier depletions by at least a factor of two for all species reported in [Table 7](#). No comet in [Table 7](#) shows an H $_2$ O/CO ratio < 20%, a limit two orders of magnitude higher than the observed value in R2 PanSTARRS, and most have H $_2$ O/CO \gtrsim 100%. It should also be noted that there is a tendency for comets observed at large heliocentric distance to be

Table 6. Additional Mixing Ratios for R2 PanSTARRS

Species	X/CO ₂ (%)	X/CH ₄ (%)	X/CH ₃ OH (%)	X/H ₂ CO (%)	X/HCN (%)
CH ₄	5.8 ± 0.9 (19)	-			
CH ₃ OH	11.6 ± 1.4 (13)	200 ± 28 (250)	-		
H ₂ CO	0.47 ± 0.09 (1.9)	8.0 ± 1.6 (38)	4.0 ± 0.7 (15)	-	
HCN	0.04 ± 0.01 (1.3)	0.71 ± 0.20 (25)	0.36 ± 0.09 (10)	8.9 ± 2.6 (67)	-
C ₂ H ₆	< 0.89 (3.7)	< 15 (72)	< 7.6 (29)	< 190 (190)	< 2125 (290)
C ₂ H ₂	< 0.21 (0.94)	< 3.8 (18)	< 1.9 (7.2)	< 47 (48)	< 525 (72)
NH ₃	< 0.1 (5.4)	< 1.8 (103)	< 0.9 (41)	< 22 (276)	< 250 (414)

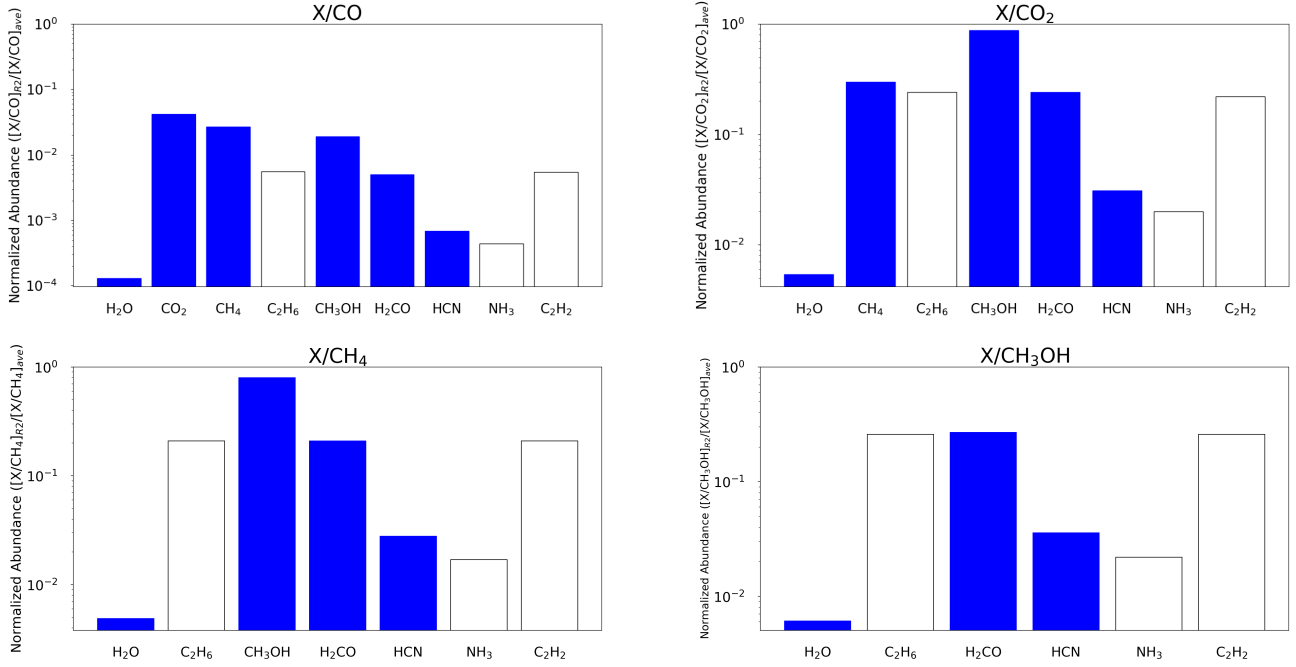


Figure 11. Comparison of the volatile composition of C/2016 R2 (PanSTARRS) to the average comet for mixing ratios relative to four of the five most abundant ices in R2 PanSTARRS: CO (top left), CO₂ (top right), CH₄ (bottom left), and CH₃OH (bottom right). The upper limit of each plot is unity, indicating a “typical” composition compared to other comets observed to date. A white histogram with black outline denotes an upper limit, while blue indicates a detected value. It is clear that no matter what species is used as the standard the composition of R2 PanSTARRS deviates from the average comet by at least a factor of three for almost all species whose abundances are constrained with sufficient sensitivity. The exceptions are CH₃OH/CO₂ and CH₃OH/CH₄, which have values only 10-20% below the average values for the ensemble of comets observed to date. OCS and N₂ are omitted due to a lack of sufficiently well defined average values for the cometary population, but the large N₂ abundance (third most abundant volatile detected) certainly suggests that N₂ is enriched relative to all species when compared to other comets.

highly active, which is potentially attributed to being CO-rich. Therefore the general overabundance of CO compared to other volatiles for comets observed at large heliocentric distance could simply be due to this observational bias. 29P/Schwassman-Wachmann 1 shows the most similarities with R2 PanSTARRS, with an H₂O/CO ratio \sim 20%, low abundances of CH₄ and C₂H₆ compared to CO, and a reported N₂/CO ratio of \sim 1% (Ivanova et al. 2016). However, at 6.2 AU the CO sublimation rate is expected to be \sim 10,000 times faster than the H₂O sublimation rate (Cowan and A’Hearn 1979), so accounting for this sublimation effect implies that the intrinsic H₂O/CO ratio in the nucleus of 29P may be more in line with that typically observed in comets (H₂O/CO > 300%) (Womack et al. 2017). The upper limits on species such as CH₄/CO and HCN/CO are not sensitive enough to show whether 29P is similar to R2

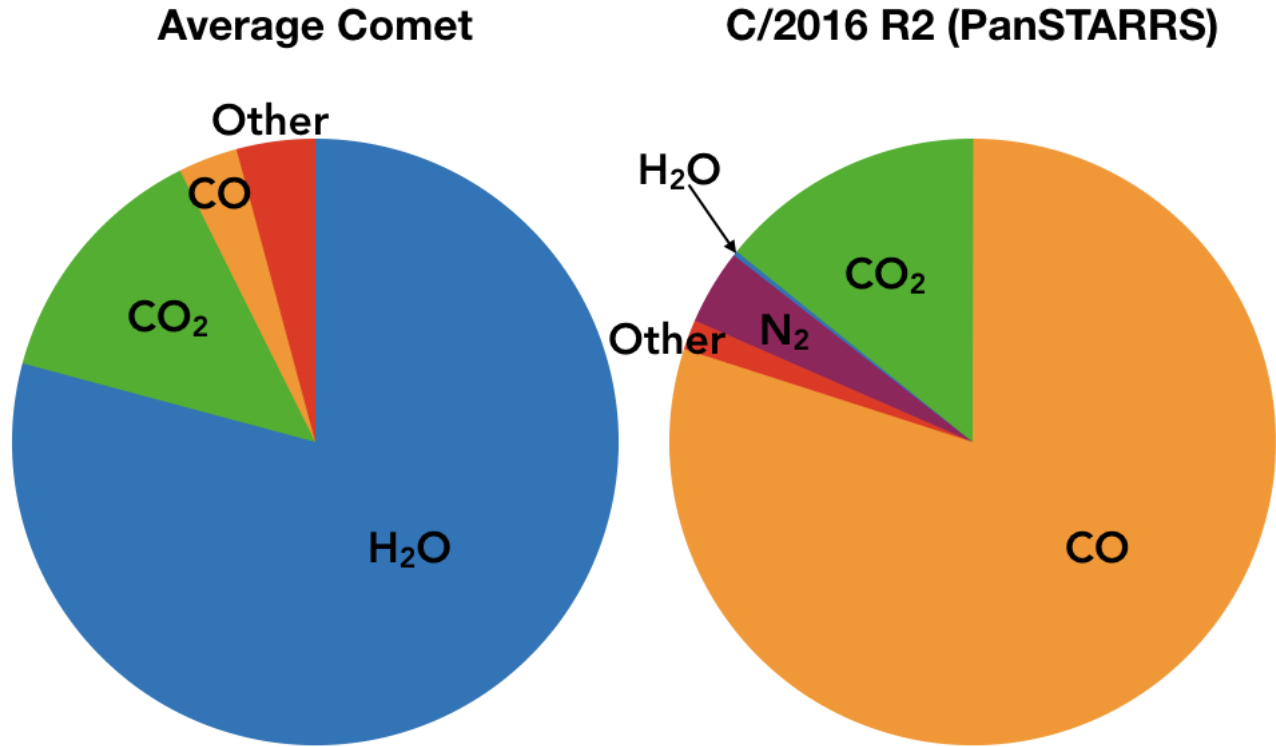


Figure 12. Comparison of the volatile composition of C/2016 R2 (PanSTARRS) to the average comet as derived using mixing ratios from Dello Russo et al. (2016a) and Ootsubo et al. (2012). The dominance of CO and large amount of N₂ makes R2 PanSTARRS unique among comets observed with modern capabilities inside the water ice line.

PanSTARRS, as these upper limits are at least one order of magnitude larger than the observed abundances in R2 PanSTARRS.

Probably the best studied comet at large heliocentric distance is 67P/Churyumov-Gerasimenko, for which *in situ* measurements with the ROSINA mass spectrometer aboard Rosetta are available (Le Roy et al. 2015; Rubin et al. 2015a). Values for the winter and summer hemispheres at 3.14 AU pre-perihelion are presented in Table 7. Similar to the other comets in Table 7, both hemispheres exhibit abundances different from R2 PanSTARRS by at least a factor of three, with H₂O, CO₂, HCN, and C₂H₆ exhibiting the most striking differences. The N₂/CO ratio for 67P is approximately a factor of 10 smaller than the value for R2 PanSTARRS (Rubin et al. 2015a), which combined with the CO/H₂O ratios given in Table 7 implies an N₂/H₂O ratio for R2 PanSTARRS four to five orders of magnitude larger than that for 67P.

Moderate enhancements in CO compared to H₂O are expected based on the sublimation model of Cowan and A'Hearn (1979), which predicts that the different volatilities of CO and H₂O can account for a factor of two at a heliocentric distance of 2.8 AU, similar to the enhancement observed in other comets near 3 AU but not the factor of $\sim 10,000$ observed for R2 PanSTARRS. Therefore the anomalous mixing ratios cannot be ascribed to the heliocentric distance alone and must reflect the intrinsic composition of the nucleus.

4.4. Active Fractions

Our derived active areas and active fractions for H₂O, CO₂, and CO are given in Table 4. While the nucleus size of R2 PanSTARRS is not known, the very large active area required for CO would require the nucleus to be quite large (> 5 km) for all the CO to come from surface sublimation. There is also the possibility of an extended source of CO, which adds additional available surface area for CO to sublimate from. However, our *Spitzer* data (which is sensitive to both CO and CO₂ as discussed earlier) do not show evidence for increasing production rate with photometric aperture size, as would be expected for an extended source (Combi et al. 2013; Bodewits et al. 2014; McKay et al. 2015), arguing against an extended source larger than $\sim 10,000$ km in radius (corresponding to ~ 5 pixels in our *Spitzer* images, the smallest photometric aperture for which reliable photometry can be performed) for these molecules. We

Table 7. R2 PanSTARRS and Other Comets Observed at Large Heliocentric Distance

Comet	R_h (AU)	Q_{CO} (10^{27} mol s $^{-1}$)	Mixing Ratios X/CO (%)					
			H ₂ O	CO ₂	CH ₄	C ₂ H ₆	HCN	CH ₃ OH
C/2006 W3 ^a	3.13	19.8 ± 2.0	102 ± 15	43 ± 6	-	-	-	-
C/2006 W3 ^b	3.26	55.5 ± 2.6	-	-	4.4 ± 0.4	2.1 ± 0.2	-	-
C/2006 W3 ^c	3.20	39.0 ± 3.0	-	-	-	-	0.42 ± 0.04	3.8 ± 0.8
29P ^a	6.18	29.1 ± 2.1	21.6 ± 2.4	< 1.1	-	-	-	-
29P ^d	6.26	26.7 ± 2.8	< 1830	-	< 4.8	< 2.2	< 5.2	< 35.3
C/2010 G2 ^e	2.50	4.7 ± 0.7	93 ± 20	-	9.0 ± 0.9	3.8 ± 0.4	-	-
C/1995 O1 ^f	2.93	230	140	32	-	-	-	-
C/1995 O1 ^g	2.84	200	300 ± 39	-	-	-	0.58 ± 0.10	7.1 ± 0.7
C/2006 OF2 ^a	3.2	< 0.45	> 377	> 220	-	-	-	-
C/2006 Q1 ^a	2.78	< 0.37	> 973	> 432	-	-	-	-
C/2007 G1 ^a	2.80	< 0.32	> 563	> 131	-	-	-	-
C/2007 Q3 ^a	3.29	< 0.40	> 1000	> 175	-	-	-	-
C/2008 Q3 ^a	2.96	< 0.39	> 179	> 115	-	-	-	-
67P ^h	3.14	~ 0.01 ⁱ	3700	93	4.8	11.9	3.3	11.5
67P ^j	3.14	~ 0.01 ⁱ	500	400	2.8	16.5	3.1	2.8
C/2016 R2 ^k	2.8	95.4 ± 9.1	0.32 ± 0.04	18.2 ± 3.5	0.59 ± 0.09	< 0.089	(3.8 ± 1.0) × 10 ⁻³	1.04 ± 0.08

a Ootsubo et al. (2012)

b Bonev et al. (2017)

c Bockelée-Morvan et al. (2010)

d Paganini et al. (2013)

e Kawakita et al. (2014), spectra obtained after outburst

f Crovisier et al. (1997)

g Biver et al. (2018)

h Le Roy et al. (2015), Summer Hemisphere

i Le Roy et al. (2015) do not provide production rates, therefore we adopt the approximate CO production rate from (Fougere et al. 2016), their Fig. 11.

j Le Roy et al. (2015), Winter Hemisphere

k Values are those shown in Table 5

cannot definitively rule out the possibility of an extended source of smaller spatial extent than our Spitzer photometric apertures, though our modeling of the CO spatial profile in our iSHELL observations using only optical depth effects (see Section 3.1) provides some evidence against a smaller extended source.

The derived H₂O active fraction is consistent with other comets if the nucleus is fairly small (< 3 km), but this would contradict the large active area needed to explain the CO production. For a large nucleus (> 10 km) this would imply a very low active fraction for H₂O sublimation, much lower than other comets (Sosa and Fernández 2011; Lis et al. 2019). This is additional evidence that the low water production is not simply an artifact of the large heliocentric distance of R2 PanSTARRS at the time of observation, but is part of the inherent composition of this comet.

4.5. Implications

R2 PanSTARRS has an extremely anomalous composition compared to other comets observed to date. In the previous sections we have demonstrated that the large heliocentric distance can only explain a small portion of the observed composition. Additionally, the depletion of highly volatile species like CO₂ and CH₄ compared to CO cannot be explained by the heliocentric distance either. Therefore the observed anomalous abundances are not a consequence solely of the heliocentric distance. It is not likely due to thermal evolution from repeated solar passages, as this would work to deplete the most volatile species like CO, N₂, CH₄, and CO₂, not enhance them as observed. Therefore the composition of R2 PanSTARRS likely reflects its composition when it was formed.

CO and N₂ are the most primitive molecular forms of carbon and nitrogen, respectively, in the universe. They often

are the starting point of chemical pathways that result in the formation of more complex molecules such as CH_3OH , NH_3 and HCN . Therefore the large abundance of CO and N_2 in R2 PanSTARRS compared to these more complex molecules suggests that the region of the disk where R2 PanSTARRS formed was chemically inactive, and shielded from photodestruction, leaving the volatile carbon and nitrogen in their simplest forms. Both CO and N_2 are also extremely volatile, as are CH_4 and CO_2 . The presence of these molecules suggests that R2 PanSTARRS must have formed in the farthest reaches of the protosolar disk in order to retain these hypervolatiles. The presence of these hypervolatiles also suggests little depletion of these ices from repeated solar passages, despite R2 PanSTARRS likely not being dynamically new and therefore having likely experienced at least several passages through the planetary region (A dynamical analysis by [Opitom et al. \(2019\)](#) found that 100% of their 1000 R2 clones experienced at least three perihelion passages of less than 3 AU). [Wierchos and Womack \(2018\)](#) propose that the CO , N_2 and HCN relative abundances in the coma may be explained by the comet forming in an environment $\sim 50\text{K}$ (though other models suggest N_2 requires colder temperatures around 20K to condense out of the gas phase ([Drozdovskaya et al. 2016](#))) with significant shielding for N_2 . Our observations showing very high N_2 , with very low NH_3 abundances may provide additional support for this model, and thus the comet may more closely resemble the composition of the nitrogen-bearing volatiles of dense molecular clouds ([Womack et al. 1992](#)) and YSO's ([Gibb et al. 2004](#)). The large abundance of CO and CO_2 in R2 PanSTARRS is typical of interstellar apolar ice mantles, and high N_2 abundances are also expected in these ice mantles ([Gibb et al. 2004](#)). However, interstellar ice grains also have an abundant polar component that has a large water ice abundance, resulting in H_2O ice being the dominant component of ISM ice grains ([Gibb et al. 2004](#)), unlike what we observe for R2 PanSTARRS.

Of the observed species, our measurements suggest that the dominant carbon-bearing molecules are CO and CO_2 , while the dominant nitrogen-bearing molecule is N_2 . While CO and CO_2 are the main reservoirs of volatile carbon in comets, NH_3 and to a lesser extent HCN are typically the dominant reservoirs of volatile nitrogen in comets. Assuming CO and CO_2 contain the majority of the volatile carbon and N_2 the volatile nitrogen in R2 PanSTARRS implies a C/N ratio of ~ 11 , while most comets, for which NH_3 is the main volatile nitrogen carrier, have a higher C/N ratio of ~ 20 . The solar value for C/N is ~ 3.4 ([Lodders 2010](#)), so while R2 PanSTARRS has a C/N ratio closer to solar than most comets observed to date, its coma is still deficient in nitrogen compared to the Sun.

Our results show that most of the volatile oxygen in R2 PanSTARRS is locked in CO and CO_2 , not H_2O as is typically the case. This may suggest that R2 PanSTARRS formed in a region of the protosolar nebula where the C/O ratio > 1 , as chemical models predict that when carbon is more abundant than oxygen in the gas phase most oxygen will be locked into CO and CO_2 , leaving little oxygen to form H_2O . However, there is also evidence from both comets and protosolar disk models that most of the water in the Solar System was inherited from the presolar cloud rather than formed in the protosolar disk ([Cleeves et al. 2014](#); [Altwegg et al. 2017](#)). If accurate, then the lack of H_2O in R2 PanSTARRS could reveal details of how inherited H_2O was distributed throughout the protosolar disk, i.e. whether H_2O was distributed heterogeneously throughout the disk. Another possible reservoir for volatile oxygen is O_2 , which was detected with a surprisingly large abundance by the Rosetta spacecraft at comet 67P/Churyumov-Gerasimenko ([Bieler et al. 2015](#); [Keeney et al. 2017](#)) and also in archival data from the Giotto spacecraft at 1P/Halley ([Rubin et al. 2015b](#)). O_2 is extremely difficult to detect remotely, and none of our observations are sensitive to O_2 , so we cannot rule out the presence of a large amount of O_2 in R2 PanSTARRS. Production of O_2 at 67P was found to correlate well with H_2O production ([Bieler et al. 2015](#); [Fougere et al. 2016](#)), and because of this some theories for the origin of O_2 in comets invoke a strong tie to H_2O , either through radiolysis or trapping in clathrates (e.g. [Mousis et al. 2016](#); [Dulieu et al. 2017](#); [Laufer et al. 2017](#)). Given the very low H_2O abundance in R2 PanSTARRS, this would suggest the O_2 abundance should also be very low. However, given the very peculiar chemistry of R2 PanSTARRS and our limited understanding of O_2 incorporation into cometary nuclei, we do not consider this argument definitive proof against a substantial O_2 abundance in R2 PanSTARRS.

All these implications only apply to the volatile component of R2 PanSTARRS. There are no constraints on the composition of the refractory component (i.e. dust), so we cannot make any conclusions about atomic abundances in the bulk (i.e. dust and ice) composition of R2 PanSTARRS.

[Biver et al. \(2018\)](#) suggest that R2 PanSTARRS may be a fragment of a differentiated Kuiper Belt body in order to explain the large observed hypervolatile abundances. The relative abundances of CO , CH_4 , and N_2 we observe for R2 PanSTARRS do not match surface spectra of Pluto ([Protopapa et al. 2008](#)), though the relationship between the surface composition and interior of large KBO's like Pluto is unclear. A detailed analysis of the dynamics of creating collisional fragments in the Kuiper Belt after differentiation and then dynamically transporting these fragments to the

Oort Cloud (as well as the expected volatile composition of such fragments) must be further investigated.

Such an anomalous composition brings up the possibility that R2 PanSTARRS has an interstellar origin. While the current orbit of R2 PanSTARRS does not suggest an interstellar origin, R2 PanSTARRS could be a comet captured from another Oort Cloud in the Sun’s birth cluster (or a more distant planetary system, though this is less likely) during the Solar System’s earliest stages. Interstellar origins have also been suggested for other comets with peculiar compositions such as 96P/Machholz (Schleicher 2008) and C/1988 Y1 (Yanaka) (Fink 1992). It has been shown that there could have been exchange of comets between Oort Clouds in the Sun’s birth cluster (Levison et al. 2010). However, it is not clear whether these comets would be expected to be significantly different compositionally from “solar” comets as both they and their host stars would have formed from the same nebular gas.

5. CONCLUSION

We present IR, optical, and millimeter wavelength observations of comet C/2016 R2 (PanSTARRS) and show it has a very peculiar composition compared to typical comets, with strong enhancements in species such as CO and N₂ and strong depletions in species such as H₂O and HCN, as revealed by previous studies. We determined through observations of a suite of 12 species that the anomalous composition of R2 PanSTARRS is not reserved for one or two species, but exhibits strong deviations from typical comets for most species and reference points (i.e comparing to H₂O, CO, CH₄, CH₃OH, etc.). The lone exceptions are CH₃OH/CO₂ and CH₃OH/CH₄, which are considered typical. We also show that the peculiar composition of R2 PanSTARRS is not due solely to the large heliocentric distance at the time of observation, and is intrinsic to the comet. What implications R2 PanSTARRS has for our knowledge of the early Solar System are still unclear. We suggest some future lines of research that could shed light on this issue.

1) Dynamical modeling of R2 PanSTARRS: This includes both its recent history as investigated by Opitom et al. (2019), but also dynamical simulation of the Scattered Disk to evaluate the suggestion of Biver et al. (2018) that R2 PanSTARRS could be a collisional fragment from a differentiated Kuiper Belt Object. Models would need to evaluate the likelihood of forming a differentiated KBO, collisionally fragmenting this KBO, then dynamically transporting this fragment to the Oort Cloud.

2) Chemical modeling of protosolar disks: We believe that if R2 PanSTARRS is not a collisional fragment of a differentiated KBO, it provides a new constraint on chemical models of protosolar disks. H₂O in the early Solar System was likely inherited from the parent molecular cloud (Cleeves et al. 2014). Could this create a depletion mechanism for H₂O in certain regions of the protosolar disk where R2 PanSTARRS formed? Is there a region of the protosolar disk where CO and N₂ are not efficiently processed into more complex species in order to account for the strong enhancement of these species in R2 PanSTARRS? These are only a couple questions that chemical modeling of protoplanetary disks and observations of other protoplanetary disks can help answer.

3) Continued compositional studies of comets: R2 PanSTARRS is a case-in-point for the importance of remote sensing observations to measure the composition of as many comets as possible. R2 PanSTARRS was a not particularly bright comet and was at a large heliocentric distance, meaning it could have easily been missed by compositional studies. More observations of comets are needed to determine how common comets like R2 PanSTARRS are. As pointed out by Biver et al. (2018), the closest comparisons in the historical literature are C/1908 R1 (Morehouse) and C/1961 R1 (Humason), but neither of these were studied with modern capabilities, therefore very little is known about their overall composition. With current sky surveys like PanSTARRS and LSST coming on line in the coming years, the prospect for discovering more comets like R2 PanSTARRS grows. The frequency of objects like R2 PanSTARRS will provide meaningful constraints on its history and the formation of our Solar System.

We are grateful to the anonymous reviewer for helpful comments that improved the quality of this manuscript. We thank *Spitzer*, IRTF, Apache Point Observatory, and the Discovery Channel Telescope for granting us DDT or ToO time to conduct the observations described in this paper. We thank Svetlana Jorstad for graciously allowing us to interrupt her program with our DCT ToO observations. These results made use of the Discovery Channel Telescope at Lowell Observatory. Lowell is a private, non-profit institution dedicated to astrophysical research and public appreciation of astronomy and operates the DCT in partnership with Boston University, the University of Maryland, the University of Toledo, Northern Arizona University and Yale University. The Large Monolithic Imager was built by

Lowell Observatory using funds provided by the National Science Foundation (AST-1005313). The SMT is operated by the ARO, the Steward Observatory, and the University of Arizona, with support through the NSF University Radio Observatories program grant AST-1140030. This work was completed with the GILDAS CLASA software: <http://www.iram.fr/IRAMFR/GILDAS>. The authors recognize and acknowledge the very significant cultural role and reverence that the summit of Maunakea has always had within the indigenous Hawaiian community. We are most fortunate to have the opportunity to conduct observations from this mountain. AJM acknowledges support from the NASA Postdoctoral Program, administered by the Universities Space Research Association. MD acknowledges support through NASA grant 15-SSO15_2-0028. MMK acknowledges support from NASA Solar System Observations Program grant 80NSSC18K0856. MW and KW acknowledge support from NSF grant AST-1615917. OHP acknowledges support from the USF Genshaft Family Doctoral Fellowship. BPB acknowledges support from NSF grant AST-1616306. BPB, NDR, and RJV acknowledge support from NASA Solar System Observations grant 80NSSC17K0705. NR acknowledges support from the NASA Earth and Space Science Fellowship Program (Grant NNX16AP49H). ALC acknowledges support from the NASA Solar System Observations Program (NNX17A186G).

Facilities: *Spitzer* IRAC, NASA IRTF iSHELL, ARC 3.5-meter, Discovery Channel Telescope, Arizona Radio Observatory (SMT)

REFERENCES

- M. F. A’Hearn, D. G. Schleicher, R. L. Millis, P. D. Feldman, and D. T. Thompson. Comet Bowell 1980b. *Astronomical Journal*, 89:579–591, April 1984. <https://doi.org/10.1086/113552>.
- M. F. A’Hearn, R. L. Millis, D. G. Schleicher, D. J. Osip, and P. V. Birch. The ensemble properties of comets: Results from narrowband photometry of 85 comets, 1976–1992. *Icarus*, 118:223–270, December 1995. <https://doi.org/10.1006/icar.1995.1190>.
- K. Altwegg, H. Balsiger, J. J. Berthelier, A. Bieler, U. Calmonte, J. De Keyser, B. Fiethe, S. A. Fuselier, S. Gasc, T. I. Gombosi, T. Owen, L. Le Roy, M. Rubin, T. Sémon, and C.-Y. Tzou. D₂O and HDS in the coma of 67P/Churyumov-Gerasimenko. *Philosophical Transactions of the Royal Society of London Series A*, 375:20160253, May 2017. <https://doi.org/10.1098/rsta.2016.0253>.
- J. M. Bauer, R. Stevenson, E. Kramer, A. K. Mainzer, T. Grav, J. R. Masiero, Y. R. Fernández, R. M. Cutri, J. W. Dailey, F. J. Masci, K. J. Meech, R. Walker, C. M. Lisse, P. R. Weissman, C. R. Nugent, S. Sonnett, N. Blair, A. Lucas, R. S. McMillan, E. L. Wright, t. WISE, and NEOWISE Teams. The NEOWISE-Discovered Comet Population and the CO+CO₂ production rates. *ArXiv e-prints*, September 2015.
- A. Bhardwaj and S. Raghuram. A Coupled Chemistry-emission Model for Atomic Oxygen Green and Red-doublet Emissions in the Comet C/1996 B2 Hyakutake. *Astrophysical Journal*, 748:13, March 2012. <https://doi.org/10.1088/0004-637X/748/1/13>.
- A. Bieler, K. Altwegg, H. Balsiger, A. Bar-Nun, J.-J. Berthelier, P. Bochslers, C. Briois, U. Calmonte, M. Combi, J. de Keyser, E. F. van Dishoeck, B. Fiethe, S. A. Fuselier, S. Gasc, T. I. Gombosi, K. C. Hansen, M. Hässig, A. Jäckel, E. Kopp, A. Korth, L. Le Roy, U. Mall, R. Maggiolo, B. Marty, O. Mousis, T. Owen, H. Rème, M. Rubin, T. Sémon, C.-Y. Tzou, J. H. Waite, C. Walsh, and P. Wurz. Abundant molecular oxygen in the coma of comet 67P/Churyumov-Gerasimenko. *Nature*, 526:678–681, October 2015. <https://doi.org/10.1038/nature15707>.
- N. Biver, D. Bockelée-Morvan, G. Paubert, R. Moreno, J. Crovisier, J. Boissier, E. Bertrand, H. Boussier, F. Kugel, A. McKay, N. D. Russo, and M. A. DiSanti. The extraordinary composition of the blue comet C/2016 R2 (PanSTARRS). *Astronomy and Astrophysics*, 619:A127, November 2018. <https://doi.org/10.1051/0004-6361/201833449>.
- D. Bockelée-Morvan, J. Crovisier, M. J. Mumma, and H. A. Weaver. *The composition of cometary volatiles*, pages 391–423. 2004.

- D. Bockelée-Morvan, P. Hartogh, J. Crovisier, B. Vandenbussche, B.M. Swinyard, N. Biver, D.C. Lis, C. Jarchow, R. Moreno, D. Hutsemékers, E. Jehin, M. Küppers, L.M. Lara, E. Lellouch, J. Manfroid, M. de Val-Borro, S. Szutowicz, M. Banaszekiewicz, F. Bensch, M.I. Blecka, M. Emprechtinger, T. Encreanz, T. Fulton, M. Kidger, M. Rengel, C. Waelkens, E. Bergin, G.A. Blake, J.A.D.L. Blommaert, J. Cernicharo, L. Decin, P. Encrenaz, T. de Graauw, S. Leeks, A.S. Medvedev, D. Naylor, R. Schieder, and N. Thomas. A study of the distant activity of comet C/2006 W3 (Christensen) with Herschel and ground-based radio telescopes. *Astronomy and Astrophysics*, 518:L149+, 2010.
- D. Bodewits, T. L. Farnham, M. F. A’Hearn, L. M. Feaga, A. McKay, D. G. Schleicher, and J. M. Sunshine. The Evolving Activity of the Dynamically Young Comet C/2009 P1 (Garradd). *Astrophysical Journal*, 786:48, May 2014. <https://doi.org/10.1088/0004-637X/786/1/48>.
- B. P. Bonev, M. J. Mumma, M. A. DiSanti, N. Dello Russo, K. Magee-Sauer, R. S. Ellis, and D. P. Stark. A Comprehensive Study of Infrared OH Prompt Emission in Two Comets. I. Observations and Effective g-Factors. *ApJ*, 653:774–787, December 2006. <https://doi.org/10.1086/508452>.
- B. P. Bonev, G. L. Villanueva, M. A. DiSanti, H. Boehnhardt, M. Lippi, E. L. Gibb, L. Paganini, and M. J. Mumma. Beyond 3 au from the Sun: The Hypervolatiles CH₄, C₂H₆, and CO in the Distant Comet C/2006 W3 (Christensen). *Astronomical Journal*, 153: 241, May 2017. <https://doi.org/10.3847/1538-3881/aa64dd>.
- L. I. Cleeves, E. A. Bergin, C. M. O. ’. Alexander, F. Du, D. Graninger, K. I. Öberg, and T. J. Harries. The ancient heritage of water ice in the solar system. *Science*, 345:1590–1593, September 2014. <https://doi.org/10.1126/science.1258055>.
- A. L. Cochran and A. J. McKay. Strong CO⁺ and $\{\{\rm{N}}\}\}_{-2}^{+}$ Emission in Comet C/2016 R2 (Pan-STARRS). *ApJL*, 854:L10, February 2018. <https://doi.org/10.3847/2041-8213/aaab57>.
- A. L. Cochran, E. S. Barker, and C. L. Gray. Thirty years of cometary spectroscopy from McDonald Observatory. *Icarus*, 218:144–168, March 2012. <https://doi.org/10.1016/j.icarus.2011.12.010>.
- A.L. Cochran. Atomic oxygen in the comae of comets. *Icarus*, 198(1):181–188, 2008.
- A.L. Cochran and W.D. Cochran. A high spectral resolution atlas of comet 122P/de Vico. *Icarus*, 157(2): 297–308, 2002.
- M. R. Combi and U. Fink. A Critical Study of Molecular Photodissociation and CHON Grain Sources for Cometary C 2. *Astrophysical Journal*, 484:879, July 1997. <https://doi.org/10.1086/304349>.
- M. R. Combi, J. T. T. Mäkinen, J.-L. Bertaux, E. Quémerais, S. Ferron, and N. Fougere. Water production rate of Comet C/2009 P1 (Garradd) throughout the 2011-2012 apparition: Evidence for an icy grain halo. *Icarus*, 225:740–748, July 2013. <https://doi.org/10.1016/j.icarus.2013.04.030>.
- J. J. Cowan and M. F. A’Hearn. Vaporization of comet nuclei - Light curves and life times. *Moon and Planets*, 21:155–171, October 1979. <https://doi.org/10.1007/BF00897085>.
- J. Crovisier, K. Leech, D. Bockelee-Morvan, T. Y. Brooke, M. S. Hanner, B. Altieri, H. U. Keller, and E. Lellouch. The spectrum of Comet Hale-Bopp (C/1995 01) observed with the Infrared Space Observatory at 2.9 AU from the Sun. *Science*, 275:1904–1907, March 1997. <https://doi.org/10.1126/science.275.5308.1904>.
- M. de Val-Borro, S. N. Milam, M. A. Cordiner, S. B. Charnley, G. L. Villanueva, and Y.-J. Kuan. CO-activity in comet C/2016 R2 (PANSTARRS). *The Astronomer’s Telegram*, 11254, February 2018.
- V. Debout, D. Bockelée-Morvan, and V. Zakharov. A radiative transfer model to treat infrared molecular excitation in cometary atmospheres. *Icarus*, 265: 110–124, February 2016. <https://doi.org/10.1016/j.icarus.2015.10.013>.
- A. Decock, E. Jehin, D. Hutsemékers, and J. Manfroid. Forbidden oxygen lines in comets at various heliocentric distances. *Astronomy and Astrophysics*, 555:A34, July 2013. <https://doi.org/10.1051/0004-6361/201220414>.
- A. Decock, E. Jehin, P. Rousselot, D. Hutsemékers, J. Manfroid, S. Raghuram, A. Bhardwaj, and B. Hubert. Forbidden oxygen lines at various nucleocentric distances in comets. *Astronomy and Astrophysics*, 573:A1, January 2015. <https://doi.org/10.1051/0004-6361/201424403>.
- N. Dello Russo, M. A. DiSanti, M. J. Mumma, K. Magee-Sauer, and T. W. Rettig. Carbonyl Sulfide in Comets C/1996 B2 (Hyakutake) and C/1995 O1 (Hale-Bopp): Evidence for an Extended Source in Hale-Bopp. *Icarus*, 135:377–388, October 1998. <https://doi.org/10.1006/icar.1998.5990>.
- N. Dello Russo, M.J. Mumma, M.A. DiSanti, K. Magee-Sauer, E.L. Gibb, B.P. Bonev, I.S. McLean, and L. Xu. A high-resolution infrared spectral survey of comet C/1999 H1 Lee. *Icarus*, 184(1):255–276, 2006.

- N. Dello Russo, R. J. Vervack, Jr., C. M. Lisse, H. A. Weaver, H. Kawakita, H. Kobayashi, A. L. Cochran, W. M. Harris, A. J. McKay, N. Biver, D. Bockelée-Morvan, and J. Crovisier. The Volatile Composition and Activity of Comet 103P/Hartley 2 During the EPOXI Closest Approach. *Astrophysical Journal Letters*, 734:L8+, June 2011. <https://doi.org/10.1088/2041-8205/734/1/L8>.
- N. Dello Russo, H. Kawakita, R. J. Vervack, and H. A. Weaver. Emerging trends and a comet taxonomy based on the volatile chemistry measured in thirty comets with high-resolution infrared spectroscopy between 1997 and 2013. *Icarus*, 278:301–332, November 2016a. <https://doi.org/10.1016/j.icarus.2016.05.039>.
- N. Dello Russo, R. J. Vervack, H. Kawakita, A. Cochran, A. J. McKay, W. M. Harris, H. A. Weaver, C. M. Lisse, M. A. DiSanti, H. Kobayashi, N. Biver, D. Bockelée-Morvan, J. Crovisier, C. Opitom, and E. Jehin. The compositional evolution of C/2012 S1 (ISON) from ground-based high-resolution infrared spectroscopy as part of a worldwide observing campaign. *Icarus*, 266:152–172, March 2016b. <https://doi.org/10.1016/j.icarus.2015.11.030>.
- K. A. Dick. The auroral 2150 Å feature - A contribution from lines of singly ionized atomic nitrogen. *Geophysical Research Letters*, 5:273, April 1978. <https://doi.org/10.1029/GL005i004p00273>.
- M. A. DiSanti, M. J. Mumma, N. Dello Russo, and K. Magee-Sauer. Carbon Monoxide Production and Excitation in Comet C/1995 O1 (Hale-Bopp): Isolation of Native and Distributed CO Sources. *Icarus*, 153:361–390, October 2001. <https://doi.org/10.1006/icar.2001.6695>.
- M. A. DiSanti, M. J. Mumma, N. Dello Russo, K. Magee-Sauer, and D. M. Griep. Evidence for a dominant native source of carbon monoxide in Comet C/1996 B2 (Hyakutake). *Journal of Geophysical Research (Planets)*, 108:5061, June 2003. <https://doi.org/10.1029/2002JE001961>.
- M. A. DiSanti, G. L. Villanueva, L. Paganini, B. P. Bonev, J. V. Keane, K. J. Meech, and M. J. Mumma. Pre- and post-perihelion observations of C/2009 P1 (Garradd): Evidence for an oxygen-rich heritage? *Icarus*, 228:167–180, January 2014. <https://doi.org/10.1016/j.icarus.2013.09.001>.
- M. A. DiSanti, B. P. Bonev, N. Dello Russo, R. J. Vervack, Jr., E. L. Gibb, N. X. Roth, A. J. McKay, H. Kawakita, L. M. Feaga, and H. A. Weaver. Hypervolatiles in a Jupiter-family Comet: Observations of 45P/Honda-Mrkos-Pajdušáková Using iSHELL at the NASA-IRTF. *Astronomical Journal*, 154:246, December 2017. <https://doi.org/10.3847/1538-3881/aa8639>.
- Maria N. Drozdovskaya, Catherine Walsh, Ewine F. van Dishoeck, Kenji Furuya, Ulysse Marboeuf, Amaury Thiabaud, Daniel Harsono, and Ruud Visser. Cometary ices in forming protoplanetary disc midplanes. *MNRAS*, 462(1):977–993, Oct 2016. <https://doi.org/10.1093/mnras/stw1632>.
- F. Dulieu, M. Minissale, and D. Bockelée-Morvan. Production of O₂ through dismutation of H₂O₂ during water ice desorption: a key to understanding comet O₂ abundances. *A&A*, 597:A56, Jan 2017. <https://doi.org/10.1051/0004-6361/201628445>.
- T. L. Farnham, D. G. Schleicher, and M. F. A'Hearn. The HB Narrowband Comet Filters: Standard Stars and Calibrations. *Icarus*, 147:180–204, September 2000. <https://doi.org/10.1006/icar.2000.6420>.
- M.C. Festou. The density distribution of neutral compounds in cometary atmospheres I - models and equations. *Astronomy and Astrophysics*, 95(1):69–79, 1981.
- M.C. Festou and P.D. Feldman. The forbidden oxygen lines in comets. *Astronomy and Astrophysics*, 103(1):154–159, 1981.
- U. Fink. Comet Yanaka (1988r) - A new class of carbon-poor comet. *Science*, 257:1926–1929, September 1992. <https://doi.org/10.1126/science.257.5078.1926>.
- U. Fink. A taxonomic survey of comet composition 1985–2004 using CCD spectroscopy. *Icarus*, 201:311–334, May 2009. <https://doi.org/10.1016/j.icarus.2008.12.044>.
- N. Fougere, K. Altwegg, J.-J. Berthelier, A. Bieler, D. Bockelée-Morvan, U. Calmonte, F. Capaccioni, M. R. Combi, J. De Keyser, V. Debout, S. Erard, B. Fiethe, G. Filacchione, U. Fink, S. A. Fuselier, T. I. Gombosi, K. C. Hansen, M. Hässig, Z. Huang, L. Le Roy, C. Leyrat, A. Migliorini, G. Piccioni, G. Rinaldi, M. Rubin, Y. Shou, V. Tenishev, G. Toth, and C.-Y. Tzou. Direct Simulation Monte Carlo modelling of the major species in the coma of comet 67P/Churyumov-Gerasimenko. *MNRAS*, 462:S156–S169, November 2016. <https://doi.org/10.1093/mnras/stw2388>.

- E. L. Gibb, D. C. B. Whittet, A. C. A. Boogert, and A. G. G. M. Tielens. Interstellar Ice: The Infrared Space Observatory Legacy. *ApJS*, 151:35–73, March 2004. <https://doi.org/10.1086/381182>.
- E. L. Gibb, B. P. Bonev, G. Villanueva, M. A. DiSanti, M. J. Mumma, E. Sudholt, and Y. Radeva. Chemical Composition of Comet C/2007 N3 (Lulin): Another “Atypical” Comet. *Astrophysical Journal*, 750:102, May 2012. <https://doi.org/10.1088/0004-637X/750/2/102>.
- C. Haridass, C. V. V. Prasad, and S. P. Reddy. The comet-tail (A-X) system of CO(+) - Precise molecular constants of its $2\Sigma^+$, A 2Π , and B $2\Sigma^+$ states. *Astrophysical Journal*, 388:669–677, April 1992. <https://doi.org/10.1086/171183>.
- C. Haridass, C. V. V. Prasad, and S. P. Reddy. The Comet-Tail ($A^2\Pi_i-X^2\Sigma^+$) System of $^{12}C^{16}O^+$: A Reinvestigation. *Journal of Molecular Spectroscopy*, 199: 180–187, February 2000. <https://doi.org/10.1006/jmsp.1999.7995>.
- P. Hily-Blant, V. Magalhaes, J. Kastner, A. Faure, T. Forveille, and C. Qi. Direct evidence of multiple reservoirs of volatile nitrogen in a protosolar nebula analogue. *A&A*, 603:L6, July 2017. <https://doi.org/10.1051/0004-6361/201730524>.
- D. W. Hogg, D. P. Finkbeiner, D. J. Schlegel, and J. E. Gunn. A Photometricity and Extinction Monitor at the Apache Point Observatory. *Astronomical Journal*, 122: 2129–2138, October 2001. <https://doi.org/10.1086/323103>.
- W.F. Huebner, J.J. Keady, and S.P. Lyon. Solar photo rates for planetary atmospheres and atmospheric pollutants. *Astrophysics and Space Science*, 195(1): 1–289, 291–294, 1992.
- O. V. Ivanova, I. V. Luk'yanyk, N. N. Kiselev, V. L. Afanasiev, E. Picazzio, O. Cavichia, A. A. de Almeida, and S. M. Andrievsky. Photometric and spectroscopic analysis of Comet 29P/Schwassmann-Wachmann 1 activity. *Planetary and Space Science*, 121:10–17, February 2016. <https://doi.org/10.1016/j.pss.2015.12.001>.
- David Jewitt and Karen J. Meech. Cometary Grain Scattering versus Wavelength, or, “What Color Is Comet Dust?”. *ApJ*, 310:937, Nov 1986. <https://doi.org/10.1086/164745>.
- H. Kawakita, N. Dello Russo, R. Vervack, Jr., H. Kobayashi, M. A. DiSanti, C. Opitom, E. Jehin, H. A. Weaver, A. L. Cochran, W. M. Harris, D. Bockelée-Morvan, N. Biver, J. Crovisier, A. J. McKay, J. Manfroid, and M. Gillon. Extremely Organic-rich Coma of Comet C/2010 G2 (Hill) during its Outburst in 2012. *ApJ*, 788:110, June 2014. <https://doi.org/10.1088/0004-637X/788/2/110>.
- B. A. Keeney, S. A. Stern, M. F. A’Hearn, J.-L. Bertaux, L. M. Feaga, P. D. Feldman, R. A. Medina, J. W. Parker, J. P. Pineau, E. Schindhelm, A. J. Steffl, M. Versteeg, and H. A. Weaver. H₂O and O₂ absorption in the coma of comet 67P/Churyumov-Gerasimenko measured by the Alice far-ultraviolet spectrograph on Rosetta. *Monthly Notices of the Royal Astronomical Society*, 469: S158–S177, July 2017. <https://doi.org/10.1093/mnras/stx1426>.
- M. S. P. Kelley, C. E. Woodward, D. Bodewits, T. L. Farnham, M. S. Gudipati, D. E. Harker, D. C. Hines, M. M. Knight, L. Kolokolova, A. Li, I. de Pater, S. Protopapa, R. W. Russell, M. L. Sitko, and D. H. Wooden. Cometary Science with the James Webb Space Telescope. 128(1):018009, January 2016. <https://doi.org/10.1088/1538-3873/128/959/018009>.
- M. M. Knight and D. G. Schleicher. Observations of Comet ISON (C/2012 S1) from Lowell Observatory. *Astronomical Journal*, 149:19, January 2015. <https://doi.org/10.1088/0004-6256/149/1/19>.
- C.-H. Kuo, I. W. Milkman, T. C. Steimle, and J. T. Moseley. Spectroscopy of N₂(+) Meinel bands and CO(+) comet tail bands. *Journal of Chemical Physics*, 85:4269–4275, October 1986. <https://doi.org/10.1063/1.451799>.
- S. Laine, editor. *IRAC Instrument Handbook*. Spitzer Science Center, Pasadena, 2015. URL <http://irsa.ipac.caltech.edu/data/SPITZER/docs/irac/iracinstrumenthandbook/>.
- L. E. Langland-Shula and G. H. Smith. The Unusual Spectrum of Comet 96P/Machholz. *Astrophysical Journal Letters*, 664:L119–L122, August 2007. <https://doi.org/10.1086/520839>.
- Diana Laufer, Akiva Bar-Nun, and Adi Ninio Greenberg. Trapping mechanism of O₂ in water ice as first measured by Rosetta spacecraft. *MNRAS*, 469:S818–S823, Jul 2017. <https://doi.org/10.1093/mnras/stx3359>.

- Léna Le Roy, Kathrin Altwegg, Hans Balsiger, Jean-Jacques Berthelier, Andre Bieler, Christelle Briois, Ursina Calmonte, Michael R. Combi, Johan De Keyser, and Frederik Dhooghe. Inventory of the volatiles on comet 67P/Churyumov-Gerasimenko from Rosetta/ROSINA. *A&A*, 583:A1, Nov 2015. <https://doi.org/10.1051/0004-6361/201526450>.
- H. F. Levison, M. J. Duncan, R. Brasser, and D. E. Kaufmann. Capture of the Sun's Oort Cloud from Stars in Its Birth Cluster. *Science*, 329:187–190, June 2010. <https://doi.org/10.1126/science.1187535>.
- D. C. Lis, D. Bockelée-Morvan, R. Güsten, N. Biver, J. Stutzki, Y. Delorme, C. Durán, H. Wiesemeyer, and Y. Okada. Terrestrial deuterium-to-hydrogen ratio in water in hyperactive comets. *arXiv e-prints*, April 2019.
- K. Lodders. Solar System Abundances of the Elements. *Astrophysics and Space Science Proceedings*, 16:379, 2010.
- B. L. Lutz, M. Womack, and R. M. Wagner. Ion abundances and implications for photochemistry in Comets Halley (1986 III) and Bradfield (1987 XXIX). *Astrophysical Journal*, 407:402–411, April 1993. <https://doi.org/10.1086/172523>.
- L. Magnani and M. F. A'Hearn. CO(+) fluorescence in comets. *Astrophysical Journal*, 302:477–487, March 1986. <https://doi.org/10.1086/164006>.
- D. Makovoz and I. Khan. Mosaicking with MOPEX. In P. Shopbell, M. Britton, and R. Ebert, editors, *Astronomical Data Analysis Software and Systems XIV*, volume 347 of *Astronomical Society of the Pacific Conference Series*, page 81, December 2005.
- A. J. McKay, N. J. Chanover, J. P. Morgenthaler, A. L. Cochran, W. M. Harris, and N. D. Russo. Forbidden oxygen lines in Comets C/2006 W3 Christensen and C/2007 Q3 Siding Spring at large heliocentric distance: Implications for the sublimation of volatile ices. *Icarus*, 220:277–285, July 2012. <https://doi.org/10.1016/j.icarus.2012.04.030>.
- A. J. McKay, N. J. Chanover, J. P. Morgenthaler, A. L. Cochran, W. M. Harris, and N. D. Russo. Observations of the forbidden oxygen lines in DIXI target Comet 103P/Hartley. *Icarus*, 222:684–690, February 2013. <https://doi.org/10.1016/j.icarus.2012.06.020>.
- A. J. McKay, N. J. Chanover, M. A. DiSanti, J. P. Morgenthaler, A. L. Cochran, W. M. Harris, and N. D. Russo. Rotational variation of daughter species production rates in Comet 103P/Hartley: Implications for the progeny of daughter species and the degree of chemical heterogeneity. *Icarus*, 231:193–205, March 2014. <https://doi.org/10.1016/j.icarus.2013.11.029>.
- A. J. McKay, A. L. Cochran, M. A. DiSanti, G. Villanueva, N. D. Russo, R. J. Vervack, J. P. Morgenthaler, W. M. Harris, and N. J. Chanover. Evolution of H₂O, CO, and CO₂ production in Comet C/2009 P1 Garradd during the 2011-2012 apparition. *Icarus*, 250:504–515, April 2015. <https://doi.org/10.1016/j.icarus.2014.12.023>.
- A. J. McKay, M. S. P. Kelley, A. L. Cochran, D. Bodewits, M. A. DiSanti, N. D. Russo, and C. M. Lisse. The CO₂ abundance in Comets C/2012 K1 (PanSTARRS), C/2012 K5 (LINEAR), and 290P/Jäger as measured with Spitzer. *Icarus*, 266:249–260, March 2016. <https://doi.org/10.1016/j.icarus.2015.11.004>.
- A. J. McKay, D. Bodewits, and J.-Y. Li. Observational constraints on water sublimation from 24 Themis and 1 Ceres. *Icarus*, 286:308–313, April 2017. <https://doi.org/10.1016/j.icarus.2016.09.032>.
- A. J. McKay, A. L. Cochran, M. A. DiSanti, N. Dello Russo, H. Weaver, R. J. Vervack, W. M. Harris, and H. Kawakita. Evolution of H₂O production in comet C/2012 S1 (ISON) as inferred from forbidden oxygen and OH emission. *Icarus*, 309:1–12, July 2018. <https://doi.org/10.1016/j.icarus.2018.02.024>.
- J.P. Morgenthaler, W.M. Harris, F. Scherb, C. Anderson, R.J. Oliverson, N.E. Doane, M.R. Combi, M.L. Marconi, and W.H. Smyth. Large aperture [O I] 6300 Å photometry of comet Hale-Bopp: Implications for the photochemistry of OH. *Astrophysical Journal*, 563(1): 451–461, 2001.
- O. Mousis, T. Ronnet, B. Brugger, O. Ozgurel, F. Pauzat, Y. Ellinger, R. Maggiolo, P. Wurz, P. Vernazza, and J. I. Lunine. Origin of Molecular Oxygen in Comet 67P/Churyumov-Gerasimenko. *ApJL*, 823(2):L41, Jun 2016. <https://doi.org/10.3847/2041-8205/823/2/L41>.
- M. J. Mumma and S. B. Charnley. The Chemical Composition of Comets - Emerging Taxonomies and Natal Heritage. *Annual Review of Astronomy and Astrophysics*, 49:471–524, September 2011. <https://doi.org/10.1146/annurev-astro-081309-130811>.
- M. J. Mumma, N. Dello Russo, M. A. DiSanti, K. Magee-Sauer, R. E. Novak, S. Brittain, T. Rettig, I. S. McLean, D. C. Reuter, and L.-H. Xu. Organic Composition of C/1999 S4 (LINEAR): A Comet Formed Near Jupiter? *Science*, 292:1334–1339, May 2001. <https://doi.org/10.1126/science.1058929>.

- M. J. Mumma, B. P. Bonev, G. L. Villanueva, L. Paganini, M. A. DiSanti, E. L. Gibb, J. V. Keane, K. J. Meech, G. A. Blake, R. S. Ellis, M. Lippi, H. Boehnhardt, and K. Magee-Sauer. Temporal and Spatial Aspects of Gas Release During the 2010 Apparition of Comet 103P/Hartley 2. *ApJL*, 734:L7, June 2011. <https://doi.org/10.1088/2041-8205/734/1/L7>.
- T. Ootsubo, H. Kawakita, S. Hamada, H. Kobayashi, M. Yamaguchi, F. Usui, T. Nakagawa, M. Ueno, M. Ishiguro, T. Sekiguchi, J.-i. Watanabe, I. Sakon, T. Shimonishi, and T. Onaka. AKARI Near-infrared Spectroscopic Survey for CO₂ in 18 Comets. *Astrophysical Journal*, 752:15, June 2012. <https://doi.org/10.1088/0004-637X/752/1/15>.
- C. Opitom, D. Hutsemékers, E. Jehin, P. Rousselot, F. J. Pozuelos, J. Manfroid, Y. Moulane, M. Gillon, and Z. Benkhaldoun. High resolution optical spectroscopy of the N₂-rich comet C/2016 R2 (PanSTARRS). *A&A*, 624:A64, April 2019. <https://doi.org/10.1051/0004-6361/201834357>.
- L. Paganini, M. J. Mumma, H. Boehnhardt, M. A. DiSanti, G. L. Villanueva, B. P. Bonev, M. Lippi, H. U. Käufl, and G. A. Blake. Ground-Based Infrared Detections of CO in the Centaur-comet 29P/Schwassmann-Wachmann 1 at 6.26 AU from the Sun. *Astrophysical Journal*, 766:100, April 2013. <https://doi.org/10.1088/0004-637X/766/2/100>.
- R. W. B. Pearse and A. G. Gaydon. *The identification of molecular spectra*. 1976.
- S. Protopapa, H. Boehnhardt, T. M. Herbst, D. P. Cruikshank, W. M. Grundy, F. Merlin, and C. B. Olkin. Surface characterization of Pluto and Charon by L and M band spectra. *A&A*, 490:365–375, October 2008. <https://doi.org/10.1051/0004-6361:200809994>.
- J. Rayner, T. Bond, M. Bonnet, D. Jaffe, G. Muller, and A. Tokunaga. iSHELL: a 1-5 micron cross-dispersed R=70,000 immersion grating spectrograph for IRTF. In *Ground-based and Airborne Instrumentation for Astronomy IV*, volume 8446 of *SPIE*, page 84462C, September 2012. <https://doi.org/10.1117/12.925511>.
- J. Rayner, A. Tokunaga, D. Jaffe, M. Bonnet, G. Ching, M. Connelley, D. Kokubun, C. Lockhart, and E. Warmbier. iSHELL: a construction, assembly and testing. In *Ground-based and Airborne Instrumentation for Astronomy VI*, volume 9908 of *SPIE*, page 990884, August 2016. <https://doi.org/10.1117/12.2232064>.
- W. T. Reach, S. T. Megeath, M. Cohen, J. Hora, S. Carey, J. Surace, S. P. Willner, P. Barmby, G. Wilson, W. Glaccum, P. Lowrance, M. Marengo, and G. G. Fazio. Absolute Calibration of the Infrared Array Camera on the Spitzer Space Telescope. *PASP*, 117:978–990, September 2005. <https://doi.org/10.1086/432670>.
- W. T. Reach, M. S. Kelley, and J. Vaubaillon. Survey of cometary CO₂, CO, and particulate emissions using the Spitzer Space Telescope. *Icarus*, 226:777–797, September 2013. <https://doi.org/10.1016/j.icarus.2013.06.011>.
- N. X. Roth, E. L. Gibb, B. P. Bonev, M. A. DiSanti, N. Dello Russo, R. J. Vervack, Jr., A. J. McKay, and H. Kawakita. A Tale of “Two” Comets: The Primary Volatile Composition of Comet 2P/Encke Across Apparitions and Implications for Cometary Science. *AJ*, 156:251, December 2018. <https://doi.org/10.3847/1538-3881/aae0f7>.
- M. Rubin, K. Altwegg, H. Balsiger, A. Bar-Nun, J. J. Berthelier, A. Bieler, P. Bochslers, C. Briois, U. Calmonte, and M. Combi. Molecular nitrogen in comet 67P/Churyumov-Gerasimenko indicates a low formation temperature. *Science*, 348(6231):232–235, Apr 2015a. <https://doi.org/10.1126/science.aaa6100>.
- M. Rubin, K. Altwegg, E. F. van Dishoeck, and G. Schwehm. Molecular Oxygen in Oort Cloud Comet 1P/Halley. *Astrophysical Journal Letters*, 815:L11, December 2015b. <https://doi.org/10.1088/2041-8205/815/1/L11>.
- D. G. Schleicher. The Extremely Anomalous Molecular Abundances of Comet 96p/Machholz 1 from Narrowband Photometry. *Astronomical Journal*, 136:2204–2213, November 2008. <https://doi.org/10.1088/0004-6256/136/5/2204>.

- C. Snodgrass, M. F. A'Hearn, F. Aceituno, V. Afanasiev, S. Bagnulo, J. Bauer, G. Bergond, S. Besse, N. Biver, D. Bodewits, H. Boehnhardt, B. P. Bonev, G. Borisov, B. Carry, V. Casanova, A. Cochran, B. C. Conn, B. Davidsson, J. K. Davies, J. de León, E. de Mooij, M. de Val-Borro, M. Delacruz, M. A. DiSanti, J. E. Drew, R. Duffard, N. J. T. Edberg, S. Faggi, L. Feaga, A. Fitzsimmons, H. Fujiwara, E. L. Gibb, M. Gillon, S. F. Green, A. Guijarro, A. Guilbert-Lepoutre, P. J. Gutiérrez, E. Hadamcik, O. Hainaut, S. Haque, R. Hedrosa, D. Hines, U. Hopp, F. Hoyo, D. Hutsemékers, M. Hyland, O. Ivanova, E. Jehin, G. H. Jones, J. V. Keane, M. S. P. Kelley, N. Kiselev, J. Kleyna, M. Kluge, M. M. Knight, R. Kokotanekova, D. Koschny, E. A. Kramer, J. J. López-Moreno, P. Lacerda, L. M. Lara, J. Lasue, H. J. Lehto, A. C. Lvasseur-Regourd, J. Licandro, Z. Y. Lin, T. Lister, S. C. Lowry, A. Mainzer, J. Manfroid, J. Marchant, A. J. McKay, A. McNeill, K. J. Meech, M. Micheli, I. Mohammed, M. Monguió, F. Moreno, O. Muñoz, M. J. Mumma, P. Nikolov, C. Opitom, J. L. Ortiz, L. Paganini, M. Pajuelo, F. J. Pozuelos, S. Protopapa, T. Pursimo, B. Rajkumar, Y. Ramanjooloo, E. Ramos, C. Ries, A. Riffeser, V. Rosenbush, P. Rousselot, E. L. Ryan, P. Santos-Sanz, D. G. Schleicher, M. Schmidt, R. Schulz, A. K. Sen, A. Somero, A. Sota, A. Stinson, J. M. Sunshine, A. Thompson, G. P. Tozzi, C. Tubiana, G. L. Villanueva, X. Wang, D. H. Wooden, M. Yagi, B. Yang, B. Zaprudin, and T. J. Zegmott. The 67P/Churyumov-Gerasimenko observation campaign in support of the Rosetta mission. *Philosophical Transactions of the Royal Society of London Series A*, 375:20160249, May 2017. <https://doi.org/10.1098/rsta.2016.0249>.
- A. Sosa and J. A. Fernández. Masses of long-period comets derived from non-gravitational effects - analysis of the computed results and the consistency and reliability of the non-gravitational parameters. *MNRAS*, 416:767–782, September 2011. <https://doi.org/10.1111/j.1365-2966.2011.19111.x>.
- A. T. Tokunaga, D. W. Toomey, J. Carr, D. N. B. Hall, and H. W. Epps. Design for a 1-5-micron cryogenic echelle spectrograph for the NASA IRTF. In D. L. Crawford, editor, *Instrumentation in Astronomy VII*, volume 1235 of *Proc. SPIE*, pages 131–143, July 1990. <https://doi.org/10.1117/12.19082>.
- G. L. Villanueva, M. J. Mumma, M. A. DiSanti, B. P. Bonev, E. L. Gibb, K. Magee-Sauer, G. A. Blake, and C. Salyk. The molecular composition of Comet C/2007 W1 (Boattini): Evidence of a peculiar outgassing and a rich chemistry. *Icarus*, 216:227–240, November 2011. <https://doi.org/10.1016/j.icarus.2011.08.024>.
- S.-i. Wang, R. H. Hildebrand, L. M. Hobbs, S. J. Heimsath, G. Kelderhouse, R. F. Loewenstein, S. Lucero, C. M. Rockosi, D. Sandford, J. L. Sundwall, J. A. Thorburn, and D. G. York. ARCES: an echelle spectrograph for the Astrophysical Research Consortium (ARC) 3.5m telescope. In M. Iye and A. F. M. Moorwood, editors, *Instrument Design and Performance for Optical/Infrared Ground-based Telescopes*, volume 4841 of *Society of Photo-Optical Instrumentation Engineers (SPIE) Conference Series*, pages 1145–1156, March 2003. <https://doi.org/10.1117/12.461447>.
- K. Wierzchos and M. Womack. Comet C/2016 R2 (Panstarrs). *Central Bureau Electronic Telegrams*, 4464, December 2017.
- K. Wierzchos and M. Womack. C/2016 R2 (PANSTARRS): A Comet Rich in CO and Depleted in HCN. *Astronomical Journal*, 156:34, July 2018. <https://doi.org/10.3847/1538-3881/aac6bc>.
- M. Womack, S. Wyckoff, and L. M. Ziurys. Observational constraints on solar nebula nitrogen chemistry - N₂/NH₃. *ApJ*, 401:728–735, December 1992. <https://doi.org/10.1086/172100>.
- M. Womack, G. Sarid, and K. Wierzchos. CO in Distantly Active Comets. *PASP*, 129(3):031001, March 2017. <https://doi.org/10.1088/1538-3873/129/973/031001>.